Physical and Mathematical Properties of a Quasi-Geostrophic Model of Intermediate Complexity of the Mid-Latitudes Atmospheric Circulation

Valerio Lucarini,* Antonio Speranza, and Renato Vitolo

PASEF – Physics and Applied Statistics of Earth Fluids,

Dipartimento di Matematica ed Informatica,

Università di Camerino,

Via Madonna delle Carceri,

62032 Camerino (MC), Italy†

Abstract

A quasi-geostrophic intermediate complexity model is considered, providing a schematic representation of the baroclinic conversion processes which characterize the physics of the mid-latitudes atmospheric circulation. The model is relaxed towards a given latitudinal temperature profile, which acts as baroclinic forcing, controlled by a parameter T_E determining the forced equator-to-pole temperature gradient. As T_E increases, a transition takes place from a stationary regime to a periodic regime, and eventually to an earth-like chaotic regime where evolution takes place on a strange attractor. The dependence of the attractor dimension, metric entropy, and bounding box volume in phase space is studied by varying both T_E and model resolution. The statistical properties of observables having physical relevance, namely the total energy of the system and the latitudinally averaged zonal wind, are also examined. It is emphasized that while the attractor's properties are quite sensitive to model resolution, the global physical observables depend less critically on it. For more detailed physical observables, such as the latitudinal profiles of the zonal wind, model resolution again may be critical: the effectiveness of the zonal wind convergence, acting as barotropic stabilization of the baroclinic waves, heavily relies on the details of the latitudinal structure of the fields. The necessity and complementarity of both the dynamical systems and physical approach is underlined.

PACS numbers: 05.45.-a, 47.10.+g, 47.11.+j, 47.20.-k, 47.52.+j, 92.60.-e

*Electronic address: valerio.lucarini@unicam.it

†URL: www.unicam.it/matinf/pasef

Contents

I. INTRODUCTION: ATMOSPHERIC CIRCULATION AS A PROBLEM IN PHYSICS AND IN MATHEMATICS

In the scientific context, Climate is defined by the statistical properties of the Climatic System. In its most complete definition, the Climatic system is composed of four intimately interconnected sub-systems, Atmosphere, Hydrosphere, Cryosphere, and Biosphere. These subsystems interact nonlinearly with each other on various time-space scales [1, 2].

The Atmosphere is the most rapid component of the Climatic System. The Atmosphere is very rich in microphysical structure and composition and evolves under the action of macroscopic driving and modulating agents - solar heating and Earth's rotation and gravitation, respectively. The Atmospheric Circulation is the basic engine which transforms solar heating into the energy of the atmospheric motions determining weather and climate as we commonly perceive them. The Atmosphere features both many degrees of freedom, which makes it complicated, and nonlinear interactions of several different components coupling a vast range of time-space scales, which makes it complex. In many cases, the dynamics of such a system is strongly chaotic - in the sense that the autocorrelation function of any variable vanishes on finite time scales - and is characterized by a large natural variability on different time scales [3, 4]

The understanding of the physical mechanisms operating in the Atmosphere critically influences important human activities like weather forecast, territorial planning, etc. This is one reason why, more than half a century ago, von Neumann posed the Atmospheric Circulation in the core of the ongoing development of numerical modelling [5]. However, the General Atmospheric Circulation (GAC) also poses problems of general physical nature as a realization - in fact the one we can best observe - of planetary scale thermodynamic transformations in a rotating, stratified fluid.

Historically - see the classical monograph and paper by Lorenz [6, 7] - the problem of GAC has been essentially approached in terms of time-mean circulation and the processes which generate and maintain it. Almost one century ago Jeffrey [8, 9] realized that in order to maintain the observed time-mean circulation at middle latitudes, it is necessary to take into account the momentum and heat transfer properties of the eddies, *i.e.* the fluctuating component of the atmospheric flows [10].

Among all the physical processes involved in the GAC, the so-called *baroclinic* conversion (baroclinic comes from ancient Greek: constant pressure surfaces not parallel to constant density surfaces) plays a central role because it is through this mechanism that rotating, stratified fluids convert the available potential energy [11–13], stored in the form of thermal

fluctuations, into the vorticity and kinetic energy of the air flows as we observe them. At mid-latitudes of both hemispheres, the baroclinic conversion process can be taken as responsible for the destabilization of the fixed point given by the zonally (longitudinally) symmetric Atmospheric Circulation characterized by a purely zonal wind (jet) [35]. Baroclinic unstable waves can be actually observed (see for instance [14–16]). The definition of the basic ingredients in the mechanism of baroclinic instability has been one the main successes of the dynamical Meteorology of this century [17, 18].

Within the, virtually innumerable, papers devoted to the subject of GAC, a few happened to suggest new methodologies and concepts of general interest for fundamental disciplines, such as Physics and Mathematics, as well as more empirical natural and social sciences, such as Biology, Medicine and Economics. A leading example is that of Lorenz' attractor [19]. But, apart from such exceptions, the problem of GAC has remained confined within the boundaries of Geophysical (mostly Meteorological) literature, with all the ensuing language barriers with respect to Physics and Mathematics. Also the relatively recent (last fifteen years) public attention on Climate issues has been attracted essentially on phenomenological and/or numerical modelling issues rather than on fundamental mechanisms [20]. One consequence of this cultural separation has been that, for example, the knowledge that in dynamical systems the stability properties of the time mean state do not even provide a zeroth-order approximation of the dynamical properties of the full nonlinear system has been, and still is, quite systematically ignored in specialized literature - see [21] and [22] for enlightening examples - despite both theoretical arguments [23] and simple counter-examples of physical significance [24, 25] indicated throughout the years. Note that this, somewhat methodological, issue bears relevance also in practical problems like the provision of the so-called extended range weather forecasts, which extend beyond the deterministic predictability horizon of about 10-15 days (see *e.g.* Lorenz [6, 7]). Suppose, in fact, that the forecaster was given the next month average atmospheric fields: what practical information would he derive from that? Of course, if dynamical information is stored in the average fields - for example in the form of dominant regimes of instability derivable from the stability analysis of time-mean flow [26] - we could obtain useful information from the prediction of such time mean fields. Unfortunately, as remarked above, this picture is far from being true, and the problem of extended range is still open even in terms of formulating clearly what we should forecast!

In order to address some of the above mentioned issues, in this work we consider a quasi-geostrophic model of *intermediate* complexity for the atmospheric circulation. By intermediate we mean that the number of variables (48 to 384) lies between the few degrees

of freedom of, say, the Lorenz models [19, 27], and the state-of-the-art Global Circulation Models [20], which feature over 10^6 degrees of freedom. The model used here has no seasonal cycle and provides an earth-like representation of the turbulent baroclinic jet [24, 25]. It is vertically discretized into two layers, which is the minimum for baroclinic conversion to take place [28, 29], and latitudinally discretized by a Fourier half-sine pseudo-spectral expansion up to order JT. We have used $JT = 8$, 16, 32, 64, yielding a hierarchy of quasi-geostrophic models having increasing resolution. A fundamental property of these models is semi-linearity: the eddy field is truncated to one wavenumber in the longitudinal (zonal) direction, so that the evolution equation is linear in terms of the time-varying zonal flow. This provides a dynamical meaning for the separation between zonal and eddy flow that is only geometrical - and originally just geographical - in the traditional approach: in our case the zonal flow is an integrator of the nonlinear self-interactions of the wave-field which propagates and grows linearly on the zonal flow self.

In Sec. II we present a detailed general derivation of the evolution equations for the two-level quasi-geostrophic model starting from the *ab-initio* equations and explaining the approximation involved in the derivation of the 3D quasi-geostrophic equations. This derivation allows a clear understanding of the physics involved in the considered hierarchy of quasi-geostrophic equations and is alternative to the non-dimensional formulations which are common in the meteorological literature [28]. We further obtain the equations of the one-wavenumber model examined in this study, in the form adopted for the numerical integration.

The main results of this work are presented in Sec. III and Sec. IV. We study the sensitivity of the model behavior with respect to the parameter T_E determining the forced equator-to-pole temperature gradient, which acts as baroclinic forcing. The influence of the order of (spectral) discretization in the latitudinal direction is also analyzed. For low values of T_E there occurs a transition from a stationary to a earth-like chaotic regime. Here chaotic means that an attractor is detected having a positive maximal Lyapunov exponent, *i.e.*, a *strange* attractor (see [30] for terminology). In Sec. III we characterize the transition from stationary to chaotic dynamics in terms of bifurcation theory and study the dependence on T_E and on model resolution JT of the dimension of the strange attractor, of the metric entropy, and of the volume of its bounding box in the phase space. In Sec. IV we analyze the statistical properties of two physically meaningful observables, namely the total energy of the system and the latitudinally averaged zonal wind. An inspection of the latitudinal wind profiles is also presented. In Sec. V we give our conclusive remarks and perspectives for future works.

II. THE *AB-INITIO* FORMULATION OF THE MODEL EQUATIONS OF MOTION

A. Initial Remarks

The dynamics and thermodynamics of the dry atmosphere for an observer in the Earth's uniformly rotating frame of reference is described by the following equations [1]:

$$\frac{D}{Dt}\rho + \rho\vec{\nabla}\cdot\vec{u} = 0 \tag{1}$$

$$\frac{D}{Dt}\vec{u} + 2\vec{\Omega}\times\vec{u} = -\frac{\vec{\nabla}p}{\rho} - \vec{\nabla}\Phi + \vec{F} \tag{2}$$

$$\frac{D}{Dt}h - \frac{1}{\rho}\frac{D}{Dt}p = Q + D \tag{3}$$

$$\rho = \rho\left(p, T\right). \tag{4}$$

Here ρ is the density, $\vec{u}$ is the velocity vector, Ω is the Earth's rotation angular velocity, p is the pressure, Φ is the geopotential, $\vec{F}$ is the resultant of the frictional forces per unit mass, h is the specific enthalpy, Q is the diabatic heating, D represents the effect of heat diffusion processes, and T is the temperature of the fluid. The material derivative D/Dt is defined as follows:

$$\frac{D}{Dt}\bullet = \frac{\partial}{\partial t}\bullet + \left(\vec{u}\cdot\vec{\nabla}\right)\bullet. \tag{5}$$

Equations (1)-(3) are commonly referred to as mass continuity, Navier-Stokes, and thermodynamics, respectively. They express the dynamic balances of mass, forces, and specific enthalpy of the system, while (4) is the equation of state of the fluid under consideration, which, in the case of dry air, can be well-represented as a perfect gas.

The description of the macroscopic behavior of the atmosphere is based on the systematic use of dominant balances derived on a phenomenological basis. Suitable approximations to equations (1)-(3) are obtained by assuming that the actual evolution departs only slightly from the balances. In fact, different balances have to be applied depending on the time and space scales we are focusing on. In this way, it is possible to filter out (exclude) all solutions corresponding to physical processes that are heuristically assumed to contribute only negligibly to the dynamics of the system, at the time and space scale under examination. The magnitudes of various terms the governing equations for a particular type of motion are estimated using the so-called scale analysis technique [31]. The resulting models usually give good approximation to the observed fields when sufficiently large spatial or temporal

averages are selected [1, 28, 32].

B. The hydrostatic and quasi-geostrophic approximations

For the dynamics of the atmosphere at mid-latitudes, on spatial and temporal scales comparable with or larger than those of the synoptic weather (about 1000 Km and 1 day, respectively), it is phenomenologically well-established that the hydrostatic balance is obeyed with excellent approximation [1, 28, 32]:

$$\hat{k} \cdot \vec{\nabla} p = -\rho g, \tag{6}$$

where:

$$\hat{k} = -\frac{\vec{\nabla}\Phi}{\left|\vec{\nabla}\Phi\right|} \tag{7}$$

This expresses the balance between the gravitational force and the vertical pressure gradient, the vertical direction $\hat{k}$ being defined by the gradient of Φ. Since the atmosphere is shallow with respect to the radius of the Earth, one can use the approximation $\Phi \sim gz$, where z is the local geometric vertical coordinate. The hydrostatic balance also allows the usage of p as vertical coordinate.

Moreover, in the just mentioned synoptic scales, the atmosphere is close to the geostrophic equilibrium, which is realized when the local horizontal pressure gradient exactly balances the Coriolis acceleration. In the geostrophically balanced flows, when pressure is taken as vertical coordinate, the wind can be expressed as

$$\vec{u}_g = (u_g, v_g, 0) = \frac{1}{f_0}\hat{k} \times \vec{\nabla}\Phi = \hat{k} \times \vec{\nabla}\psi_g, \tag{8}$$

where $f_0 = 2\Omega \sin\varphi$ is the the orthogonal projection of the Coriolis parameter on the surface of the planet at latitude φ and $\psi_g = \Phi/f_0$ is defined as the streamfunction of the flow. The geostrophic wind (8) is horizontal and non-divergent. This implies that the geostrophic vorticity vector is parallel to the vertical direction and its non-vanishing component can be expressed as:

$$\xi_g = \hat{k} \cdot (\nabla \times \vec{u}_g) = \frac{1}{f_0}\Delta_H \Phi = \Delta_H \psi_g, \tag{9}$$

where Δ_H is the horizontal Laplacian operator, see *e.g.* [1, 28, 32].

Equations (6) and (8) are only diagnostic, so that no information on the evolution of the system can be obtained. From the set (1)-(4) of *ab-initio* dynamic and thermodynamic

equations of the atmosphere it is possible to obtain a set of simplified prognostic equations for the synoptic weather atmospheric fields by assuming that the fluid obeys the hydrostatic balance and undergoes small departures from the geostrophic balance. Moreover, we assume that the domain is centered at mid-latitudes and it is such that f can be well-approximated by the linear expansion $f(\varphi) \sim f(\varphi_0) + 2\Omega \cos(\varphi_0)(\varphi - \varphi_0)$.

Local Cartesian coordinates (x, y) and pressure coordinate p are introduced for the horizontal and vertical directions, respectively, with x denoting the zonal and y the latitudinal coordinate. The resulting domain is periodic in x, with wavelength L_x, and bounded in y and p, yielding

$$x \in \mathbf{R}/2\pi L_x, \quad y \in [0, L_y], \quad p \in [0, p_0], \tag{10}$$

and f is approximated as $f \sim f_0 + \beta(y - L_y/2)$. In the meteorological *jargon* this is usually referred to as the *β-channel*. A sketch of the actual geographical area corresponding to the β-channel is presented in Fig. 1. We remark that in this work, in order to avoid problems in the definition of the boundary conditions of the system, due to the prescription of the interaction with the polar and the equatorial circulations at the northern and southern boundary, respectively [24], we consider a domain extending from the pole to the equator. We remark that the quasi-geostrophic approximation is not appropriate for the equatorial region, so that we do not expect to capture any realistic feature of the tropical circulation, and that the mid-latitude channel is determined by y ranging from $1/4\ L_y$ to $3/4\ L_y$, corresponding to a latitudinal belt centered about $45^o N$ with an extension of 45^o.

Proceeding further with simplifying assumptions, the equation of state $\rho = p/RT$ is adopted for (4), where R is the gas constant for dry air, so that the following relation holds:

$$\frac{\partial \psi_g}{\partial p} = -\frac{R}{f_0 p} T, \tag{11}$$

and the specific enthalpy for the dry air is expressed as $h = C_p T$. We introduce the quasi-geostrophic material derivative:

$$\frac{D_g}{Dt} \bullet = \frac{\partial}{\partial t} \bullet + \left(\vec{u}_g \cdot \vec{\nabla}\right) \bullet = \frac{\partial}{\partial t} \bullet + J(\psi_g, \bullet), \tag{12}$$

where J is the conventional Jacobian operator defined as $J(A, B) = \partial_x A \partial_y B - \partial_y A \partial_x B$. Physically, this means that advection occurs along constant pressure levels and is performed by the geostrophic wind. This yields the so-called quasi-geostrophic equations for the stream-

function ψ_g:

$$\frac{D_g}{Dt}\left(\Delta\psi_g + f_0 + \beta y\right) - f_0\frac{\partial\omega}{\partial p} = \hat{k}\cdot\vec{\nabla}\times F + \nu\left(\Delta_H\right)^2\psi_g \tag{13}$$

$$\frac{D_g}{Dt}\left(-\frac{\partial\psi_g}{\partial p}\right) + \frac{Rp}{f_0^2}\frac{T}{\Theta}\frac{\partial\Theta}{\partial p}\frac{f_0}{p^2}\omega = \kappa\Delta_H\left(-\frac{\partial\psi_g}{\partial p}\right) + \frac{R}{pf_0}\frac{Q}{C_p} \tag{14}$$

where ω is the velocity in the direction of p, the frictional forces are represented as viscous processes with diffusion constant ν, the heat diffusion is parameterized by the coefficient κ, and Θ is the potential temperature:

$$\Theta = T\left(\frac{p_0}{p}\right)^{\frac{R}{C_p}}, \tag{15}$$

which is related to the specific entropy s of the air by

$$s = C_p \ln\Theta. \tag{16}$$

The quasi-geostrophic approximation is very useful because the resulting evolution equations (13)-(14) focus on the process of slanted convection which is responsible both for the baroclinic conversion of potential energy into eddy energy and for the generation of vorticity. These are the essential ingredients underlying the generation of atmospheric disturbances at mid-latitudes [1, 6, 28, 32]

The non-geostrophic velocity component ω does not have an evolution equation and can be diagnosed from the thermodynamics equation (14). The following boundary conditions apply for the ageostrophic velocity ω:

$$\omega\left(x, y, p = 0\right) = 0 \tag{17}$$

$$\omega\left(x, y, p = p_0\right) = -E_0\xi_g\left(x, y, p = p_0\right) \tag{18}$$

where the condition at $p = p_0$ is due to the Ekman description of the coupling of the free atmosphere with the planetary boundary layer [32]. We adopt the phenomenologically-based approximation:

$$\frac{Rp}{f_0^2}\frac{T}{\Theta}\frac{\partial\Theta}{\partial p} \sim -H(p)^2, \tag{19}$$

where $H\left(p\right)$ is the vertical scale related to the stratification of the atmosphere which depends only on p. By substituting the vertical velocity ω obtained in equation (14) into

equation (13), we obtain that the quasi-geostrophic potential vorticity q_g, defined as:

$$q_g = \Delta_H \psi_g + f_0 + \beta y + \frac{\partial}{\partial p}\left(\frac{p^2}{H^2}\frac{\partial \psi_g}{\partial p}\right), \tag{20}$$

satisfies the following canonical equation [28, 32, 33]:

$$\frac{D_g}{Dt} q_g = \kappa \frac{\partial}{\partial p}\left[\frac{p^2}{H^2}\left(-\frac{\partial \psi_g}{\partial p}\right)\right] + R\frac{\partial}{\partial p}\left(\frac{p}{H^2}\frac{Q}{C_p}\right) + \nu\left(\Delta_H\right)^2 \psi_g. \tag{21}$$

The quantity q_g (as well as all of its powers) is conserved along motion if no diabatic forcing is applied ($Q = 0$) and if the diffusion and viscous effects are discarded, *e.g.* by setting in our case $\nu = \kappa = 0$.

We remind that, formally, the quasi-geostrophic equations (13)-(14) can be derived from the *ab-initio* equations (1)-(4) by retaining the zeroth and first order term in the expansion performed on the Rossby number:

$$Ro = \frac{U}{f_0 L} \ll 1, \tag{22}$$

with $\beta L \ll f_0$, where U and L are typical values of the horizontal velocity and horizontal space scale [28].

C. The two-level model

A simplified version of system (13) and (14) is produced by discretizing the vertical direction into a finite number of pressure levels. This vertical discretization approach has been first introduced by Phillips [29] and retains the baroclinic conversion process, which is the basic physical feature of the quasi-geostrophic approximation.

We refer to Fig. 2 for a sketch of the vertical geometry of the two-layer system. The streamfunction ψ_g is thus defined at pressure levels $p = p_1 = p_0/4$ and $p = p_3 = 3/4p_0$, while ω is defined at the pressure levels $p = 0$ (top boundary), $p = p_2 = p_0/2$, and $p = p_0$ (surface boundary). The pressure level pertaining to the vertical derivative of the streamfunction $\partial\psi_g/\partial p$ as well as the stratification height H is $p = p_2$. We note that $\delta p = p_3 - p_1 = p_2 =$

$p_0/2$. This system is described by the following equations of motion:

$$\frac{D_1}{Dt}\left(\Delta_H\psi_1 + f_0 + \beta y\right) - f_0\frac{\omega_2-\omega_0}{\delta p} = 0, \tag{23}$$

$$\frac{D_3}{Dt}\left(\Delta_H\psi_3 + f_0 + \beta y\right) - f_0\frac{\omega_4-\omega_2}{\delta p} = 0, \tag{24}$$

$$\frac{D_2}{Dt}\left(\frac{\psi_1-\psi_3}{\delta p}\right) - H_2^2\frac{f_0}{p_2^2}\omega_2 = \kappa\Delta_H\left(\frac{\psi_1-\psi_3}{\delta p}\right) + \frac{R}{p_2 f_0}\frac{Q_2}{C_p}, \tag{25}$$

where we have neglected the viscous dissipation by setting $\nu = 0$, dropped the g subscript for simplicity, and have adopted the notation

$$\psi_j = \psi\left(p_j\right), \;\; j = 1,3, \qquad Q_2 = Q(p_2), \tag{26}$$

$$\omega_j = \omega\left(p_j\right), \;\; j = 0,2,4, \qquad H_2 = H(p_2), \tag{27}$$

$$\frac{D_j}{Dt}\bullet = \frac{\partial}{\partial t}\bullet + J\left(\psi_j, \bullet\right) \;\; j = 1,3. \tag{28}$$

The boundary conditions (17)-(18) on the vertical velocity are implemented as

$$\omega_0 = 0, \tag{29}$$

$$\omega_4 = -E_0\Delta_H\psi_3, \tag{30}$$

where the streamfunction at the top of the boundary layer has been approximated by the streamfunction ψ_3 [28]. The streamfunction at the intermediate level p_2 is computed as average between the streamfunctions of the levels p_1 and p_3, so that the material derivative at the level p_2 can be expressed as:

$$\frac{D_2}{Dt} = \frac{1}{2}\left(\frac{D_1}{Dt} + \frac{D_3}{Dt}\right) = \frac{\partial}{\partial t}\bullet + \frac{1}{2}J\left(\psi_1+\psi_3, \bullet\right). \tag{31}$$

Along the lines of the derivation of (21)-(20), by substituting ω_2, ω_0, and ω_4 (as defined in (25), (29), and (30), respectively) into (23) and (24), we obtain the evolution equations for the quasi-geostrophic potential vorticity at the two levels:

$$\frac{D_1}{Dt}q_1 = -\frac{\kappa}{H_2^2}\Delta_H\left(\psi_1-\psi_3\right) - \frac{R}{f_0 H_2^2}\frac{Q_2}{C_p}, \tag{32}$$

$$\frac{D_3}{Dt}q_3 = -\frac{f_0 E_0}{\delta p}\Delta_H\left(\psi_1-\psi_3\right) + \frac{\kappa}{H_2^2}\Delta_H\left(\psi_1-\psi_3\right) + \frac{R}{f_0 H_2^2}\frac{Q_2}{C_p}. \tag{33}$$

Here the q_i's are defined as:

$$q_i = \Delta_H \psi_1 + f_0 + \beta y + (1 - 2\delta_{i,1}) \frac{1}{H_2^2} (\psi_1 - \psi_3), \quad i = 1, 3, \tag{34}$$

where $\delta_{i,1}$ is the Kronecker's *delta*, which is equal to 1 when the two indexes are mutually equal and 0 otherwise.

It is possible to derive the following expression for the horizontal energy density of the system:

$$e(x, y) = \frac{\delta p}{g} \left[\frac{1}{2} \left(\vec{\nabla} \psi_1 \right)^2 + \frac{1}{2} \left(\vec{\nabla} \psi_3 \right)^2 + \frac{1}{2H_2^2} (\psi_1 - \psi_3)^2 \right]. \tag{35}$$

Here the factor $\delta p/g$ is the mass per unit surface in each level, the last term and the first two terms inside the brackets represent the potential and kinetic energy, respectively, thus featuring a clear similarity with the functional form of the energy of a harmonic oscillator. We emphasize that in (35) the potential energy term is half of what reported in [28], which contains a trivial algebraic mistake in the derivation of the energy density, as discussed with the author of the book.

We choose the following simple functional form for the diabatic heating:

$$Q_2 = \nu_N C_p (T^\star - T_2) = \nu_N C_p \frac{f_0 p_2}{R} \left(\frac{2\tau^\star}{\delta p} - \frac{\psi_1 - \psi_3}{\delta p} \right), \tag{36}$$

where $\tau^\star$ has been introduced for later convenience and, consistently with equation (11), T_2 is evaluated at the pressure level 2 and is defined by

$$\frac{\psi_3 - \psi_1}{\delta p} = -\frac{R}{f_0 p_2} T_2. \tag{37}$$

The functional form of equation (36) implies that the system is relaxed towards a prescribed temperature profile $T^\star$ with a characteristic time scale of $1/\nu_N$. $T^\star$ and $\tau^\star$ are respectively defined as follows:

$$T^\star = \frac{T_E}{2} \cos\left(\frac{\pi y}{L_y} \right), \qquad \tau^\star = \frac{R}{f_0} \frac{T_E}{4} \cos\left(\frac{\pi y}{L_y} \right), \tag{38}$$

so that T_E is the forced temperature difference between the low and the high latitude border of the domain. Since we assume no time dependence for the forcing parameter T_E, we discard the seasonal effects. Considering that the thermal wind relation:

$$\frac{\partial \vec{u}_g}{\partial p} = \hat{k} \times \vec{\nabla} \frac{\partial \psi_g}{\partial p} \tag{39}$$

can be discretized as follows for the two level system:

$$\frac{\vec{u}_1 - \vec{u}_3}{\delta p} = \hat{k} \times \vec{\nabla} \frac{\psi_1 - \psi_3}{\delta p}, \tag{40}$$

we have that the diabatic forcing Q_2 in (36) causes a relaxation of the vertical gradient of the zonal wind $u_1 - u_3$ towards the following prescribed profile $2m^\star$:

$$2m^\star = \frac{R}{f_0} \frac{\pi}{L_y} \frac{T_E}{2} \sin\left(\frac{\pi y}{L_y}\right), \tag{41}$$

where the constant 2 has been introduced for later convenience. We introduce the baroclinic and barotropic components (τ, ϕ) as

$$\tau = \frac{1}{2}(\psi_1 - \psi_3), \tag{42}$$

$$\phi = \frac{1}{2}(\psi_1 + \psi_3). \tag{43}$$

From equations (32)-(33) one obtains the equations of motion for (τ, ϕ):

$$\frac{\partial}{\partial t}\Delta_H \tau - \frac{2}{H_2^2}\frac{\partial}{\partial t}\tau + J\left(\tau, \Delta_H \phi + \beta y + \frac{2}{H_2^2}\phi\right) + J(\phi, \Delta_H \tau) = \frac{2\nu_E}{H_2^2}\Delta_H(\phi - \tau) - \frac{2\kappa}{H_2^2}\Delta_H \tau + \frac{2\nu_N}{H_2^2}(\tau - \tau^\star), \tag{44}$$

$$\frac{\partial}{\partial t}\Delta_H \phi + J(\phi, \Delta_H \phi + \beta y) + J(\tau, \Delta_H \tau) = -\frac{2\nu_E}{H_2^2}\Delta_H(\phi - \tau). \tag{45}$$

where $\nu_E = f_0 E_0 H_2^2/(2\delta)$ and the meaning of $\tau^\star$ is made clear. Notice that this system only features quadratic nonlinearities. The two-level quasi-geostrophic system (44)-(45) can be brought to the non-dimensional form, which is more usual in the meteorological literature and is easily implementable in computer codes. This is achieved by introducing length and velocity scales l and u and performing a non-dimensionalization of both the system variables (x, y, t, ϕ, τ, T) (as described in Table I) and of the system constants (Table II). When assessing, as in our case, atmospheric phenomena from synoptic to planetary scales, suitable choices for the length and velocity scales are $l = 10m^6$ and $u = 10ms^{-1}$. With the choices of the constants described in table II, our system is equivalent to that of Malguzzi and Speranza [24], where the following correspondences hold:

$$\frac{1}{H_2^2} \leftrightarrow F, \quad \frac{2\nu_E}{H_2^2} \leftrightarrow \frac{\nu_E}{2}, \quad \frac{2\kappa}{H_2^2} \leftrightarrow \nu_S, \quad \text{and} \quad \nu_N \leftrightarrow \nu_H. \tag{46}$$

D. The single zonal wave two-level model

In this section we derive the evolution equations used in the present study. We Fourier-expand the ϕ and τ fields in the zonal direction x as follows:

$$\phi(x,y,t) = \sum_{n=0}^{\infty} A_n(y,t) \exp(\mathrm{i}2n\pi x/L_x) + \text{c.c.} \tag{47}$$

$$\tau(x,y,t) = \sum_{n=0}^{\infty} B_n(y,t) \exp(\mathrm{i}2n\pi x/L_x) + \text{c.c.}, \tag{48}$$

where c.c. stands for complex conjugate. By definition we have

$$U(y,t) = -\frac{\partial A_0(y,t)}{\partial y}, \qquad m(y,t) = -\frac{\partial B_0(y,t)}{\partial y}, \tag{49}$$

so that U represents the zonal average of the mean of the zonal wind at the two pressure levels 1 and 3 (see previous Section), while m represents the zonal average of the halved difference between the the zonal wind at the two pressure levels 1 and 3. In this work we focus on the interaction between the average zonal wind and waves, thus neglecting the wave-wave nonlinear interactions. We therefore only retain the zonally symmetric component (*i.e.*, that of order $n = 0$) and one of the non-zonal components (*i.e.*, for a fixed $n \geq 1$) in the Fourier expansions (47)-(48) and in the equations of motion. Since quadratic nonlinearities like those described in equations (44)-(45) generate terms with Fourier components corresponding to the sum and difference of the Fourier components of the two factors, no wave-wave interactions can take place. Note that if cubic nonlinearities were present, direct wave-wave interaction would have been possible [34]. In the present case, the wave can self-interact only indirectly through the changes in the values of the zonally symmetric fields U and m. This amounts to building up a semi-linear equation for the wave on top of a nonlinear dynamics for the zonally symmetric parts of the fields.

As the only retained non-zonal component we select that of order $n = 6$, since we intend to represent the baroclinic conversion processes, that in the real atmosphere take place on scales of $L_x/6$ or smaller [16]. With this choice, setting $\chi = 6 \times 2\pi/L_x$ in order to simplify the notation, equations (47)-(48) reduce to

$$\phi(x,y,t) = -\int_{\pi/2}^{y} U(z,t)\,\mathrm{d}z + A\exp(\mathrm{i}\chi x) + \text{c.c.}, \tag{50}$$

$$\tau(x,y,t) = -\int_{\pi/2}^{y} m(z,t)\,\mathrm{d}z + B\exp(\mathrm{i}\chi x) + \text{c.c.}, \tag{51}$$

where the choice of the lower integration limit will be explained later. By substituting (50)-(51) into equations (44)-(45) and projecting onto the Fourier modes of order $n = 0$ and $n = 6$, we obtain the equations:

$$\begin{aligned}\dot{A}_{yy} - \chi^2\dot{A} + \left(\mathrm{i}\chi U + \frac{2\nu_E}{H_2^2}\right)A_{yy} - \left(\mathrm{i}\chi^3 U + \mathrm{i}\chi U_{yy} + \frac{2\nu_E}{H_2^2}\chi^2 - \mathrm{i}\chi\beta\right)A \\ + \left(\mathrm{i}\chi m - \frac{2\nu_E}{H_2^2}\right)B_{yy} - \left(\mathrm{i}\chi^3 m + \mathrm{i}\chi m_{yy} - \frac{2\nu_E}{H_2^2}\chi^2\right)B = 0,\end{aligned} \tag{52}$$

$$\begin{aligned}\dot{B}_{yy} - \chi^2\dot{B} - \frac{2}{H_2^2}\dot{B} + \left(\mathrm{i}\chi U + \frac{2\nu_E}{H_2^2} + \frac{2\kappa}{H_2^2}\right)B_{yy} \\ - \left(\mathrm{i}\chi^3 U + \mathrm{i}\chi U_{yy} + \frac{2\nu_E}{H_2^2}\chi^2 - \mathrm{i}\chi\beta + \frac{2\kappa}{H_2^2}\chi^2 + \frac{2\nu_N}{H_2^2} + \frac{2}{H_2^2}\mathrm{i}\chi U\right)B \\ + \left(\mathrm{i}\chi m - \frac{2\nu_E}{H_2^2}\right)A_{yy} - \left(\mathrm{i}\chi^3 m + \mathrm{i}\chi m_{yy} - \frac{2\nu_E}{H_2^2}\chi^2 - \frac{2}{H_2^2}\mathrm{i}\chi m\right)A = 0,\end{aligned} \tag{53}$$

$$\dot{U} + \frac{2\nu_E}{H_2^2}(U - m) + 2\chi\,\mathrm{Im}(AA^*_{yy} + BB^*_{yy}) = 0, \tag{54}$$

$$\begin{aligned}\dot{m}_{yy} - \frac{2}{H_2^2}\dot{m} + \frac{2\kappa}{H_2^2}m_{yy} - \frac{2\nu_E}{H_2^2}(U - m)_{yy} - \frac{2\nu_N}{H_2^2}(m - m^*) \\ + \frac{4}{H_2^2}\chi\,\mathrm{Im}(A^*B)_{yy} + 2\chi\,\mathrm{Im}(AB^*_y + BA^*_y)_{yyy} = 0,\end{aligned} \tag{55}$$

where (52)-(53) and (54)-(55) refer respectively to the non-zonal and zonal components, the dot indicates time differentiation, and X^* denotes the complex conjugate of X. This is a set of 6 equations for the real fields A^1, A^2, B^1, B^2, U, m, where A^1 and A^2 are the real and imaginary parts of A and similarly for B. Rigid walls are taken as boundaries at $y = 0, L_y$, so that all fields have vanishing boundary conditions. We emphasize that, by construction, no wave-wave interactions occur in (52)-(55). Moreover, only quadratic nonlinear terms are present, due to the fact that the same holds for (44)-(45). A Fourier half-sine expansion of the fields is carried out, with time-varying coefficients:

$$A^i = \sum_{j=1}^{JT} A^i_j \sin\left(\frac{\pi j y}{L_y}\right), \;\; i = 1, 2, \tag{56}$$

$$B^i = \sum_{j=1}^{JT} B^i_j \sin\left(\frac{\pi j y}{L_y}\right), \;\; i = 1, 2, \tag{57}$$

$$U = \sum_{j=1}^{JT} U_j \sin\left(\frac{\pi j y}{L_y}\right), \tag{58}$$

$$m = \sum_{j=1}^{JT} m_j \sin\left(\frac{\pi j y}{L_y}\right), \tag{59}$$

truncating at order JT. Therefore, the lower integration limit in (50)-(51) is such that

the two fields τ and ϕ as reconstructed from (56)-(59) have automatically zero mean when latitudinally integrated. Such a choice allows for the fact that the energy density (35), and consequently the total energy of the system, does not depend on the latitudinally averaged value of τ, which has no physical relevance. We denote by $\Pi_j(\cdot)$ the projection operator onto the basis function $\sin(\frac{\pi jy}{L_y})$. Because of computational speed, we chose a collocation (also known as pseudospectral) projection, see Appendix A for a details. By linearity of $\Pi_j(\cdot)$, its action on linear terms in (52)-(55) is obvious. For example, terms like A^1_{yy} are represented as

$$A^1_{yy} = -\sum_{j=1}^{JT} w_j^2 A_j^1 \sin\left(\frac{\pi jy}{L_y}\right), \qquad \text{where } \; w_j = \frac{\pi j}{L_y}. \tag{60}$$

So by plugging expansion (56)-(59) into the equations (52)-(55), and by applying $\Pi_j(\cdot)$, we eventually obtain a set of $6 \times JT$ ordinary differential equations in the coefficients A_j^1, A_j^2, B_j^1, B_j^2, U_j, m_j, with $j = 1, \ldots, JT$:

$$\begin{aligned}\dot{A}_j^1 = \frac{1}{\chi^2 + w_j^2}\Bigg[&-\frac{2\nu_E}{H_2^2}(\chi^2 + w_j^2)A_j^1 - \chi\beta A_j^2 + \frac{2\nu_E}{H_2^2}(\chi^2 + w_j^2)B_j^1 + \\ &\Pi_j\left(-\chi U A^2_{yy} + \chi^3 U A^2 + \chi U_{yy} A^2 - \chi m B^2_{yy} + \chi^3 m B^2 + \chi m_{yy} B^2\right)\Bigg],\end{aligned} \tag{61}$$

$$\begin{aligned}\dot{A}_j^2 = \frac{1}{\chi^2 + w_j^2}\Bigg[&-\frac{2\nu_E}{H_2^2}(\chi^2 + w_j^2)A_j^2 + \chi\beta A_j^1 + \frac{2\nu_E}{H_2^2}(\chi^2 + w_j^2)B_j^2 + \\ &\Pi_j\left(\chi U A^1_{yy} - \chi^3 U A^1 - \chi U_{yy} A^1 + \chi m B^1_{yy} - \chi^3 m B^1 - \chi m_{yy} B^1\right)\Bigg],\end{aligned} \tag{62}$$

$$\begin{aligned}\dot{B}_j^1 =&\frac{1}{\chi^2 + w_j^2 + \frac{2}{H_2^2}}\Bigg[-\left(\frac{2\nu_E}{H_2^2} + \frac{2\kappa}{H_2^2}\right)(\chi^2 + w_j^2)B_j^1 - \chi\beta B_j^2 + \frac{2\nu_E}{H_2^2}(\chi^2 + w_j^2)A_j^1 + \\ &\Pi_j\left(-\chi U B^2_{yy} + \chi^3 U B^2 + \chi U_{yy} B^2 + \frac{2}{H_2^2}\chi U B^2 - \chi m A^2_{yy} + \chi^3 m A^2 + \chi m_{yy} A^2 - \frac{2}{H_2^2}\chi m A^2\right)\Bigg],\end{aligned} \tag{63}$$

$$\begin{aligned}\dot{B}_j^2 =&\frac{1}{\chi^2 + w_j^2 + \frac{2}{H_2^2}}\Bigg[-\left(\frac{2\nu_E}{H_2^2} + \frac{2\kappa}{H_2^2}\right)(\chi^2 + w_j^2)B_j^2 + \chi\beta B_j^1 + \frac{2\nu_E}{H_2^2}(\chi^2 + w_j^2)A_j^2 + \\ &\Pi_j\left(\chi U B^1_{yy} - \chi^3 U B^1 - \chi U_{yy} B^1 - \frac{2}{H_2^2}\chi U B^1 + \chi m A^1_{yy} - \chi^3 m A^1 - \chi m_{yy} A^1 + \frac{2}{H_2^2}\chi m A^1\right)\Bigg],\end{aligned} \tag{64}$$

$$\dot{U}_j = -\frac{2\nu_E}{H_2^2}(U - m) - 2\chi\Pi_j\left(-A^1 A^2_{yy} + A^2 A^1_{yy} - B^1 B^2_{yy} + B^2 B^1_{yy}\right), \tag{65}$$

$$\begin{aligned}\dot{m}_j =&\frac{1}{\frac{2}{H_2^2} + w_j^2}\Bigg[-w_j^2\frac{2\kappa}{H_2^2}m_j + w_j^2\frac{2\nu_E}{H_2^2}(U_j - m_j) - \frac{2\nu_N}{H_2^2}(m_j - m_j^*) + \\ &\Pi_j\left(4\chi\frac{1}{H_2^2}(A^1 B^2 - A^2 B^1)_{yy} + 2\chi(-A^1 B^2_{yy} + A^2 B^1_{yy} - B^1 A^2_{yy} - B^2 A^1_{yy})_{yy}\right)\Bigg].\end{aligned} \tag{66}$$

System (61)-(66) constitutes the base model of our study. For the truncation order JT we have used the values: $JT = 8, 16, 32, 64$.

III. DYNAMICAL AND STATISTICAL CHARACTERIZATION OF THE MODEL'S ATTRACTOR

A. Hadley Equilibrium

The system of equations (44)-(45) has the following stationary solution for zonally symmetric flows:

$$\phi(y) = \tau(y), \tag{67}$$

$$\frac{2\kappa}{H_2^2}\frac{d^2\tau(y)}{dt^2} + \frac{2\nu_N}{H_2^2}(\tau(y) - \tau^\star(y)) = 0. \tag{68}$$

Considering the functional form (38) for $\tau^\star(y)$, the following expression for $\tau(y)$ holds:

$$\tau(y) = \phi(y) = \frac{R}{f_0}\frac{T_E}{4}\frac{\cos\left(\frac{\pi y}{L_y}\right)}{1+\frac{\kappa}{\nu_N}\left(\frac{\pi}{L_y}\right)^2} = \frac{\tau^\star(y)}{1+\frac{\kappa}{\nu_N}\left(\frac{\pi}{L_y}\right)^2}. \tag{69}$$

When expressing this solution in terms of the average zonal wind $U(y)$ and of half of the wind shear $m(y)$, both defined in (49), we have:

$$m(y) = U(y) = \frac{R}{f_0}\frac{\pi}{L_y}\frac{T_E}{4}\frac{\sin\left(\frac{\pi y}{L_y}\right)}{1+\frac{\kappa}{\nu_N}\left(\frac{\pi}{L_y}\right)^2} = \frac{m^\star(y)}{1+\frac{\kappa}{\nu_N}\left(\frac{\pi}{L_y}\right)^2}, \tag{70}$$

where we have used the definition (41) for $m^\star(y)$. Moreover, since the temperature T_2 is proportional to τ (compare (37) and (42)), the following temperature profile $T_2(y)$ is realized:

$$T_2(y) = \frac{T_E}{2}\frac{\cos\left(\frac{\pi y}{L_y}\right)}{1+\frac{\kappa}{\nu_N}\left(\frac{\pi}{L_y}\right)^2} = \frac{T^\star(y)}{1+\frac{\kappa}{\nu_N}\left(\frac{\pi}{L_y}\right)^2}. \tag{71}$$

This solution describes a zonally symmetric circulation characterized by the instantaneous balance between the horizontal temperature gradient and the vertical wind shear, which corresponds on the Earth system to the idealized pattern of the Hadley equilibrium [28, 32, 35]. In particular, since $m(y) = U(y)$, we have that $u_1(y) = 2U(y)$ and $u_3(y) = 0$, *i.e.* all the dynamics takes place in the upper pressure level. Since the the lower pressure level experiences no motion, the Ekman sucking process is switched off and, consistently, the solution does not depend on the corresponding coupling constant ν_E.

There is a value of the equator-to-pole temperature gradient T_E^H such that if $T_E < T_E^H$

the Hadley equilibrium (67)-(70) is stable and has an infinite basin of attraction, whereas if $T_E > T_E^H$ it is unstable.

In the stable regime with $T_E < T_E^H$, after the decay of transients, the fields ϕ, τ, m, U, and T are time-independent and feature zonal symmetry - they only depend on the variable y. Moreover, they are proportional by the same near-to-unity factor to the corresponding relaxation profiles, compare (67)-(71). In particular, this implies that all the equilibrium fields are proportional to the parameter T_E.

In our model, since the forcing $m^\star(y)$ only projects onto the first latitudinal Fourier mode (see (41)), the Hadley equilibrium is fully described as follows:

$$A_j^i(t) = B_j^i(t) = 0, \quad i = 1, 2, \quad j = 1, \ldots, JT, \tag{72}$$

$$m_j(t) = U_j(t) = 0, \quad j = 2, \ldots, JT, \tag{73}$$

$$m_1(y) = U_1(y) = \frac{m^\star(y)}{1 + \frac{\kappa}{\nu_N}\left(\frac{\pi}{L_y}\right)^2}. \tag{74}$$

When increasing the values of the control parameter T_E beyond T_E^H, the equilibrium described by (67)-(68) becomes unstable. The physical reason for this, as first pointed out by Charney and Eady on vertically continuous models [17, 18] and by Phillips on the two two-level model [29], is that for high values of the meridional temperature gradient the Hadley equilibrium is unstable with respect to the process of baroclinic conversion, which allows the transfer of available potential energy of the zonal flow stored into the meridional temperature gradient into energy of the eddies, essentially transferring energy from the latter term to the first two terms of the energy density expression (35). The two-level model, as first pointed out by Phillips [29], is the minimal model allowing for the representation of this process.

At mathematical level, in our model we have that for $T_E = T_E^H$ a complex conjugate pair of eigenvalues of the linearization of (61)-(66) cross the imaginary axis so that their real part turns positive, which suggests the occurrence of a Hopf bifurcation [36].

The observed value of T_E^H changes with the considered truncation order JT. Results are reported in Table III for the choice of constants reported in Table II and for $JT = 8$, 16, 32, 64. We have that T_E^H increases with the value of JT. The reason for this is that the finer is the resolution, the more efficient are the stabilizing mechanisms which counteract the baroclinic instability. Such mechanisms are the barotropic stabilization of the jet, increasing the horizontal shear through the convergence of zonal momentum [37–40], and the viscous dissipation, which both act preferentially on the small scales since they involve the spatial

derivatives of the fields ϕ and τ. This is a clarifying example that in principle it is necessary to include suitable renormalizations in the parameters of a model when changing the resolution JT, in order to keep correspondence with the resulting dynamics [27]. Nevertheless, in our case the values of T_E^H obtained for the adopted resolutions are rather similar.

Moreover, in our model the number of linearly unstable modes of the Hadley equilibrium (67)-(70) increases with the value of T_E. As shown in Fig. 3, at each *jump* in the graphs an additional pair of complex conjugate eigenvalues crosses the imaginary axis. The increase of the number of linearly unstable modes of the Hadley equilibrium can be framed at physical level in the fact that for larger values of T_E a larger pool of available potential energy is available for conversion and faster latitudinally varying modes can become unstable, similarly to case of the Phillips model [29]. We remind that the system under investigation obeys a Squires condition [41], so that the fastest growing among the unstable modes is the latitudinally gravest one. The signature of the relevance of the stabilizing mechanisms and of the geometrical properties of the linearly unstable modes developing for higher values of JT can be confirmed by observing respectively that while for low values of T_E ($T_E \lesssim 12$) the number of linearly unstable modes decreases with JT, the converse is true for high values of T_E ($T_E \gtrsim 25$).

B. Transition to Chaos

In this section we analyze the route to the formation of a strange attractor of model (61)-(66) as the parameter T_E is increased. Throughout the section, JT is fixed at 32, but the results are similar for the other considered values of JT.

A stable periodic orbit (Fig. 4 (A)) branches off from the Hadley equilibrium (67)-(70) as T_E increases above $T_E^H \sim 8.275$. We recall that the Hadley equilibrium loses stability at T_E^H as a pair of complex conjugate eigenvalues of the linearization of (61)-(66) crosses the imaginary axis, (see previous section). This strongly suggests the occurrence of a supercritical Hopf bifurcation, which might be checked by center manifold reduction and normal form analysis (see *e.g.* [36]), but it is beyond the scope of the present work. The attracting periodic orbit persists for T_E in a narrow interval, up to approximately $T_E = 8.485$, where it disappears through a saddle-node bifurcation taking place on an attracting invariant two-torus, see Fig. 5. Intermittency of saddle-node type [42] on the two-torus is illustrated in Fig. 4 (B): after an initial transient the orbit is attracted to a quasi-periodic evolution characterized by long time-spans, resembling the periodic evolution of Fig. 4 (A), alternated by relatively short bursts in which the orbit *explores* the rest of the two-torus. In other words,

for T_E right after the saddle-node bifurcation, the orbit on the two-torus *slows down* in the phase space region where the saddle-node has taken place. This yields a higher density of points in that region, see Fig. 5.

For slightly larger values of T_E, a strange attractor develops by so-called quasi-periodic breakdown of a *doubled* torus. This is one of the most typical routes for onset of chaos (weak turbulence) in fluid dynamics experiments and low-dimensional models, compare [43–46] and references therein. We describe this route by means of a Poincaré section of the attractor of (61)-(66), obtained by intersecting an orbit with a hyperplane $U_1 = c_0$ for a suitable constant c_0. In this Poincaré section, the two-torus yields a circle ($T_E = 8.516$) which is invariant and attracting under the Poincaré (return) map, see Fig. 6 (A). At first, at $T_E = 8.52$ the two-torus loses stability through a *quasi-periodic period doubling* (see [47, Sec. 4.3] and references therein for the theory of quasi-periodic bifurcations). Thereby a period two circle attractor is created, meaning a pair of disjoint circles mapped onto each other by the Poincaré map (Fig. 6 (B)). By further increasing T_E up to $T_E = 8.521$, a second doubling occurs, where a period four circle attractor is born (Fig. 6 (C)). Then for $T_E = 8.522$ approximately a transition to chaotic motion occurs: the period four circle turns into a strange attractor having a narrow band-like structure (Fig. 6 (D)), which is likely to be a *quasi-periodic* Hénon-like strange attractor, see [44, 48]. We remark that:

- For smaller values of T_E, a sort of *doubling bubble* occurs, *i.e.* two consecutive doublings (at approximately $T_E = 8.504$ and $T_E = 8.509$) resulting in an attractor like in Fig. 6 (C), followed by two *undoublings* (at $T_E = 8.513$ and $T_E = 8.516$) where the circle attractor in Fig. 6 (A) reappears. This sort of direct-inverse finite sequence is not uncommon in dynamical systems, see *e.g.* [49].

- Both the breakdown of a quasi-periodic circle attractor and the resulting quasi-periodic Hénon-like strange attractor are dynamical phenomena occurring rather frequently but which are not completely understood from the theoretical viewpoint (see [44, 48]).

As T_E further increases, the band widens and blurs (Fig. 6 (E), for $T_E = 8.58$) until no significant structure can be visually detected (Fig. 6 (F)) for $T_E = 10$.

The statistical properties of the attractor of (61)-(66) also display a typical evolution. For values of T_E nearby the two-torus breakdown, quasi-periodic intermittency is observed, *i.e.* the autocorrelations of an *observable* (a function of state space variables) typically decay

very slowly. We consider the total energy $E(t)$ of (61)-(66), defined as:

$$E(t) = \int_0^{L_y} \int_0^{L_x} e(x, y, t) dx dy = 6 \int_0^{L} \int_0^{\frac{2\pi}{\chi}} e(x, y, t) dx dy, \tag{75}$$

where $e(x, y, t)$ is the energy density in (35) (details on the algorithm used for the computation of time series of $E(t)$ are given in Appendix A). In Fig. 7 (A), we display the lagged autocorrelation $ACF[E(t), Lag]$ of the time series of the total energy for $T_E = 8.521$, 8.522 and $T_E = 8.58$. These cases are representative of the qualitatively distinct observed behaviors. For $T_E = 8.522$ the autocorrelation is very similar to what obtained for $T_E = 8.521$, in spite of the fact that the former value corresponds to chaotic behavior whereas the latter to regular (quasi-periodic) dynamics. This occurs because for $T_E = 8.522$ the chaoticity is very weak and the quasi-periodic intermittency rather strong. A much faster decay of the autocorrelation, albeit still with the signature of intermittency, is observed for $T_E = 8.58$. The quasi-periodic intermittency for T_E near T_E^{crit} is also illustrated by the geometrical structure of the attractor, which still bears resemblance with that of the formerly existing torus. See the Poincaré sections in Fig. 6 (D) and (E).

For larger values of T_E (Fig. 7), we have that at $T_E = 9$ the autocorrelation decays quite similarly to the case $T_E = 8.58$ (the Poincaré section, not shown, is also quite similar), but already at $T_E = 10$ the quasi-periodic intermittency is no longer present (compare Fig. 6 (F)). Correspondingly, the autocorrelation decays rather quickly for $T_E = 10$ and, *a fortiori*, for $T_E = 18$. Again compare with [43–46].

Completely analogous routes to chaos occur for model (61)-(66) with $JT = 16$ and 64. However, the locations on the T_E-axis of the various bifurcations are slightly shifted with respect to the case $JT = 32$, compare Fig. 3 and Table III. Moreover, for $JT = 8$, a different route takes place, involving a quasi-periodic Hopf bifurcation of the two-torus (instead of a quasi-periodic period doubling), whereby an invariant three-torus is created. In the Poincaré section (not shown), this corresponds to an attracting two-torus.

The invariant objects involved in the transition to low-dynamical chaos described in this section correspond to well-known fluid flow patterns. In particular, the two-torus attractor in phase space yields an *amplitude vacillation* in the flow, whereas the three-torus detected for $JT = 8$ yields a *modulated amplitude vacillation*, see [46, 50] and references therein. However, a characterization of the strange attractors occurring for large T_E and of their relation to turbulence is still lacking. Typically, low-dimensional nonhyperbolic strange attractors, such as the Lorenz [19] and Hénon-Pomeau attractors [51, 52], are the topological closure of a set of unstable periodic orbits. Moreover, the Hénon-Pomeau attractor coincides with the

closure of the unstable manifold $W^u(p)$ of a fixed point p of saddle type. See *e.g.* [49, 53–55] and references therein. To the best knowledge of the authors, no similar properties has yet been proved (or even formulated) with sufficient generality for nonhyperbolic strange attractors of larger dimension.

We suspect that plenty of unstable periodic orbits and invariant tori coexist with the attractor of model (61)-(66) with $JT = 32$, for sufficiently large T_E. Indeed, from Fig. 3 we deduce that the Hadley equilibrium undergoes several other bifurcations after the first one. Since the number of unstable eigenvalues of the Hadley equilibrium increases at each Hopf bifurcation, the periodic orbits that branch off have unstable manifolds of increasingly high dimension. Moreover, these unstable periodic orbits in turn undergo Hopf bifurcations (also called torus or Neĭmark-Sacker [36]) where unstable two-tori branch off, compare [24, Sec. 5]. It seems, therefore, that the phase space quickly gets crowded with high-dimensional unstable invariant manifolds. The question remains open whether such complex dynamical characterizations of the system play a role in the geometrical structure of the strange attractor and are potentially useful for computing the statistical properties, let it go for the time average fields considered in the classical atmospheric circulations theories or the Hadley equilibrium of most theories of atmospheric instability.

C. Lyapunov Exponents and Dimension of the Strange Attractor

To characterize the dynamical properties of the strange attractors of (61)-(66) we resort to the study of the Lyapunov exponents [30, 56]. See Appendix B for a description of the algorithm used to compute them. In what follows, the Lyapunov exponents are denoted by $\lambda_1, \lambda_2, \ldots, \lambda_N$, with $\lambda_1 \geq \lambda_2 \geq \cdots \geq \lambda_N$, $N = 6 \times JT$.

In the left panel of Fig. 8 we represent the evolution of some of the 192 Lyapunov exponents of the attractor of (61)-(66) with $JT = 32$ as T_E is increased. The maximal exponent λ_1 becomes positive as T_E crosses the torus breakdown value T_E^{crit}, and then increases monotonically with T_E.

The spectrum of the Lyapunov exponents is plotted in the right panel of Fig. 8 for three different values of T_E, again with $JT = 32$. The distribution of the exponents approaches a smooth shape for large T_E and a similar shape is observed for $JT = 64$ (not shown). This suggests the existence of a well-defined *infinite baroclinicity* model obtained from (44)-(45) as a (possibly, singular perturbation) limit for $T_E \to \infty$.

1. Dimension of the Strange Attractor

The Lyapunov exponents are used to compute the Lyapunov dimension (also called Kaplan-Yorke dimension, see [30, 57]) and metric entropy (also known as Kolmogorov-Sinai entropy [30]).

The Lyapunov dimension is defined by

$$D_L = k + \frac{\sum_{j=1}^{k} \lambda_j}{|\lambda_{k+1}|}, \tag{76}$$

where k is the unique index such that $\sum_{j=1}^{k} \lambda_j \geq 0$ and $\sum_{j=1}^{k+1} \lambda_j < 0$. Under general assumptions on the dynamical system under examination, D_L is an upper bound for the Hausdorff dimension of an attractor.

We have also computed (not shown) other numerical estimates for the dimension of an attractor: the correlation and information dimensions [58]. However, these estimates become completely meaningless when the Lyapunov dimension increases beyond, say, 20. In particular, the correlation and information algorithms drastically underestimate the dimension. This is a well-known problem: for large dimensions, prohibitively long time series have to be used [50]. Ruelle [59] suggests the following rule of thumb: you need a time series of length $10^{d/2}$ to estimate an attractor of dimension d. Therefore, computational time and memory constraints in fact limit the applicability of correlation-like algorithms to low-dimensional attractors.

The number of positive Lyapunov exponents (unstable dimension [30]) increases with T_E, which implies that the Lyapunov dimension also does so. This is confirmed by a plot of the Lyapunov dimension as a function of T_E for four values of the discretization order $JT = 8$, 16, 32, and 64 (see Fig. 9). For all the considered values of JT, it is possible to distinguish three characteristic regimes in the behavior of the function $D_L(T_E)$:

- For small values of $(T_E - T_E^{crit})$, we have that $D_L \propto (T_E - T_E^{crit})^{\gamma}$, with γ ranging from ~ 0.5 ($JT = 8$) to ~ 0.7 ($JT = 64$). The range of T_E where this behavior can be detected increases with JT.

- For larger values of T_E a linear scaling regime of $D_L \sim \beta T_E + const.$ is found in all cases. The linear coefficient is for all JT remarkably close to $\beta \sim 1.2$. The domain of validity of the linear approximation is apparently homothetic, as can be seen from the simple geometric construction in figure Fig. 9.

- For T_E larger than a JT-depending threshold, there occurs a sort of phase-space

saturation as the Lyapunov dimension begins to increase sublinearly with T_E. Note that while for $JT = 8$ the model is in this regime in most of the explored T_E-domain ($T_E \gtrsim 20$), for $JT = 64$ the threshold is reached only for $T_E \gtrsim 108$. In this latter regime of parametric dependence the system is not able to provide an adequate representation of the details of the dynamics of the system. Further discussions on this point will be given in Sec. III D and Sec. IV.

2. Entropy production

The metric entropy $h(\rho)$ of an ergodic invariant measure ρ expresses the mean rate of information creation, see [30] for definition and other properties. If a dynamical system possesses a SRB (Sinai-Ruelle-Bowen) invariant measure ρ, then Pesin's identity holds:

$$h(\rho) = \sum_{\lambda_j > 0} \lambda_j. \tag{77}$$

Existence of an SRB measure for is rather difficult to show for a given nonhyperbolic attractor [30]. It has been only proven for low-dimensional cases such as the Hénon [60] or Lorenz [55] strange attractors. More generally one has the inequality $h(\rho) \geq \sum_{\lambda_j>0} \lambda_j$. We then simply *assume* the existence of a *unique* SRB measure and refer to the sum of the positive Lyapunov exponents as metric entropy.

The maximal Lyapunov exponent, the predictability time $t_p = \lambda_1^{-1}$, and the metric entropy as functions of T_E are compared for $JT = 8$, 16, 32, and 64 in Fig. 10. It turns out that, for fixed JT, λ_1 increases sublinearly with T_E, whereas for T_E fixed, λ_1 decreases for increasing values of JT. Consequently, for fixed JT the predictability time decreases monotonically with T_E. We note that, for all values of JT, if $T_E > 14$ we have that $t_p < 10$, which corresponds in physical units to a predictability time $t_p \lesssim 12$ days. Moreover, in the range $T_E \gtrsim 12$, t_p is proportional to $(T_E - T_E^{crit})^\gamma$, with γ ranging between $[-0.85, -0.8]$ depending on the considered value of JT. The metric entropy has a marked linear dependence $h \sim \beta(T_E - T_E^{crit})$, with β ranging from ~ 0.15 ($JT = 8$) to ~ 0.5 ($JT = 64$). Moreover, for a given value of T_E, the metric entropy increases with JT. From the dynamical viewpoint, this means on one hand that the maximal sensitivity of the system to variations in the initial condition along a *single direction* is largest for $JT = 8$. On the other hand, there are many more *active degrees of freedom* for $JT = 64$ and they collectively produce a faster *forgetting* of the initial condition as time goes on.

3. Parametric smoothness of the attractor properties with respect to T_E

The dependence of the Lyapunov exponents and, consequently, of the predictability time, of the Lyapunov dimension and metric entropy, with respect to T_E is remarkably smooth, especially if one keeps in mind the paradigms of low-dimensional nonhyperbolic strange attractors. For example, for the logistic mapping (see *e.g.* [30]) the maximal Lyapunov exponent λ_1 is a discontinuous function of the parameter at every point where $\lambda_1 > 0$. This is due to the fact that so-called *windows of periodicity*, that is, open parameter intervals where the logistic mapping has a periodic attractor, are *dense* in the parameter axis. In the complement set of the windows of periodicity, parameter values for which a strange attractor occurs form a nowhere dense set of positive Lebesgue measure. In fact, similar features seem to hold for many low-dimensional mappings having strange attractors, such as the Hénon-like families [52, 54, 60], also compare [30, 44, 49] and references therein.

No windows of periodicity were detected in the fully chaotic range (say, $T_E > 16$) for model (61)-(66), independently of the truncation order $JT = 8$, 16, 32, 64. We have also tried slightly different spectral discretization schemes and integration methods (such as leapfrog or Runge-Kutta 4), but this qualitative feature of smoothness and absence of windows of periodicity persisted in all cases.

There are two possible explanations for this: either the windows of periodicity are very narrow or there are no windows of periodicity. A possible theoretical support for the latter case might be provided by the concept of *robust* strange attractors. We refer the interested reader to [55] for a discussion and more references. Also see [61] for a class of low-dimensional maps where strange attractors occur on open parameter sets.

From the above it follows that, from the dynamical point of view, the model (61)-(66) behaves in sensibly different ways if the truncation order JT is changed. For example, in the earth-like regime $T_E = 18$, the Lyapunov dimension nearly doubles when passing from $JT = 32$ to $JT = 64$. However, despite the quantitative differences, many qualitative features remain the same for $JT \geq 16$:

- the route for the creation of the strange attractor involves a Hopf bifurcation of the Hadley equilibrium, followed by quasi-periodic breakdown of the invariant torus;
- a linear scaling regime exists for the Lyapunov dimension as a function of T_E;
- the maximal Lyapunov exponent and the metric entropy increase monotonically with T_E;

- the distribution of the Lyapunov exponents tends to a well-defined shape for T_E large (Fig. 8 right);
- the dependence of Lyapunov exponents, dimension and metric entropy with respect to T_E is remarkably smooth.

D. Bounding Box of the Attractor

In this section we study the volume of the bounding box V_{BB} for the attractors of model (61)-(66) previously described. The bounding box of a set of points in an $N-$dimensional space is defined as the smallest hyperparallelepiped containing the considered set [62, 63]. For clarity, in the N-dimensional phase space, where $N = 6 \times JT$, the volume V_{BB} is computed as:

$$V_{BB} = \prod_{k=1}^{N=6\times JT} \left[\max_{t_{tr}<t<t_{max}} (z_k(t)) - \min_{t_{tr}<t<t_{max}} (z_k(t)) \right]. \tag{78}$$

Here the z_k denote the $6 \times JT$ variables spanning the phase space of the system, in our case the Fourier coefficients A_j^1, A_j^2, B_j^1, B_j^2, m_j, and U_j, with $j = 1, \ldots, JT$. The condition $t > t_{tr}$ allows for the transients to die out. Typically, t_{tr} is rather safely fixed to 1500, which correspond to about five years.

When the Hadley equilibrium is the universal attractor, the volume V_{BB} is zero, while it is non-zero if the computed orbit is attracted to a periodic orbit, a two-torus or a strange attractor. In all cases V_{BB}, which represents the bulk size of the attractor in phase space, grows with T_E. More precisely, each of the factors in the product (78) increases with T_E, so that expansion occurs in all directions of the phase space. This matches the basic expectations on the behavior of a dissipative system having a stronger energy input.

In the right panel of Fig. 11 we present a plot of $\log(V_{BB})$ as function of T_E for the selected values of $JT = 8$, 16, 32, and 64. In the case $JT = 8$, V_{BB} obeys with great precision the power law $V_{BB} \propto (T_E - T_E^{crit})^\gamma$ in the whole domain $T_E \geq 9$. The best estimate for the exponent is $\gamma \sim 40$. Given that the total number of Fourier components is $6 \times JT = 48$, this implies that the growth of the each side of the bounding box is on the average proportional to about the $5/6^{th}$ power of $(T_E - T_E^{crit})$.

For higher values of JT, two sharply distinct and well defined power-law regimes occur. For $JT = 16$, in the lower range of $(T_E - T_E^{crit})$ - corresponding in all cases to $T_E \lesssim T_E^{crit} + 1.5$ - the volume of the bounding box increases with about the 35^{th} power of $(T_E - T_E^{crit})$, while

in the upper range of $(T_E - T_E^{crit})$ - for $T_E \gtrsim T_E^{crit} + 1.5$ - the power-law exponent abruptly jumps up to about 80. For $JT = 32$ the same regimes can be recognized, but the values of the best estimates of the exponents are twice as large as what obtained with $JT = 16$. Similarly, for $JT = 64$ the best estimates of the exponents are twice as large as for $JT = 32$. The results on the power law fits of $V_{BB} \propto (T_E - T_E^{crit})^{\gamma}$ are summarized in Table IV. We emphasize that in all cases the uncertainties on γ, which have been evaluated with a standard bootstrap technique, are rather low and total to less than 3% of the best estimate of γ. Moreover, the uncertainty of the power-law fit greatly worsens if we detune the value of T_E^{crit} by as little as 0.3, thus reinforcing the idea that fitting a power law against the logarithm of $(T_E - T_E^{crit})$ is a robust choice.

When considering separately the various sides of the bounding box hyperparallelepiped (not shown), *i.e.*, each of the factors in the product (78), we have that for $JT = 8$ all of them increase as about $(T_E - T_E^{crit})^{5/6}$ in the whole range. For $JT = 16$, 32, and 64, in the lower range of T_E each side of the bounding box increases as about the $1/3^{rd}$ power of $(T_E - T_E^{crit})$, while in the upper range of T_E each side of the bounding box increases as about the $5/6^{th}$ power of $(T_E - T_E^{crit})$. Selected cases are depicted in the right panel of Fig. 11. So for a given value of truncation order JT, the ratios between the ranges of the various degrees of freedom are essentially unchanged when varying T_E, so that the system obeys a sort of self-similar scaling with T_E.

Summarizing, for sufficiently high truncation order ($JT \geq 16$) a robust parametric dependence is detected for the volume of the bounding box as a function of T_E:

$$V_{BB} \propto (T_E - T_E^{crit})^{\gamma}, \quad \gamma = \epsilon N \quad \epsilon \sim \begin{cases} 1/3, & T_E - T_E^{crit} \lesssim 1.5, \\ 5/6, & T_E - T_E^{crit} \gtrsim 1.5, \end{cases} \tag{79}$$

where $N = 6 \times JT$ is the number degrees of freedom.

The comparison, for, say, $JT = 16$ and 32, of factors in (78) having the same order for the same value of $T_E - T_E^{crit}$ provides insight about the sensitivity to model resolution. In the following discussion, we examine the variables A_j^1 but similar observations apply to all other variables A_j^2, B_j^1, B_j^2, U_j, and m_j. The factors related to the the gravest modes, such as $\left[\max\left(A_j^1(t)\right) - \min\left(A_1^1(t)\right)\right]$, agree with high precision, thus suggesting that the large scale behavior of the system is only slightly affected by variation of model resolution. When considering the terms related to the fastest latitudinally varying modes allowed by both truncation orders, such as $\left[\max\left(A_j^1(t)\right) - \min\left(A_j^1(t)\right)\right]$ with $17 \leq j \leq 32$, we have that those obtained for $JT = 32$ are *larger* than the corresponding factors obtained for $JT = 64$,

and the distance between pairs of the same order increases with j. See the right panel of Fig. 11. This is likely to be the effect of spectral aliasing [64]: the fastest modes of the model with lower resolution *absorb* the dynamics contained in the scales which are instead resolved in the higher-resolution model. The same effect is observed when comparing, for $JT = 16$ and 32, coefficients of the same order such as $\left[\max\left(A_j^1(t)\right) - \min\left(A_j^1(t)\right)\right]$ with $9 \leq j \leq 16$. The $JT = 8$ case does not precisely match this picture.

IV. STATISTICAL PROPERTIES OF THE TOTAL ENERGY AND LATITUDINALLY AVERAGED ZONAL WIND

In this section the model (61)-(66) is studied by means of observables (functions of state space variables) of physical significance, as opposed to the quantities derived from the Lyapunov exponents and the volume of the bounding box used in Sec. III C, which are more typical indicators used in dynamical systems analysis.

A. Total energy

The total energy of the system $E(t)$ defined in (75) isa very relevant observable of physical significance for the system. In Table I we report its conversion factor between the non-dimensional and dimensional units. For the Hadley equilibrium, the time-independent expression for the total energy is derived by plugging (69) into (35) and then computing the integral (75):

$$\overline{E(t)} = \frac{\delta p}{g} L_x L_y \left(\frac{R T_E}{4 f_0} \frac{1}{1 + \frac{\kappa}{\nu_E} \left(\frac{\pi}{L_y} \right)^2} \right)^2 \left(\frac{\pi^2}{L_y^2} + \frac{1}{H_2^2} \right). \tag{80}$$

The total energy is proportional to T_E^2 and is mostly stored as potential energy [1], which is described by the second term of the sum in (80).

In Fig. 12 we present the results obtained for the various values of JT used in this work. In the left panel we present the $JT = 64$ case, which is representative of what obtained also in the other cases. The time-averaged total energy is monotonically increasing with T_E, but when the system enters the chaotic regime, $\overline{E(t)}$ is much lower than the value at the coexisting Hadley equilibrium. This behavior may be related to the much larger dissipation fuelled by the chaos-driven activation of the smaller scales. In the chaotic regime $E(t)$ is characterized by temporal variability, which becomes more and more pronounced for larger values of T_E.

In the right panel of Fig. 12 we compare the cases $JT = 8, 16, 32$ with respect to $JT = 64$. The overall agreement of $\overline{E(t)}$ is good but progressively worsens when decreasing JT: for $JT = 32$, the maximal fractional difference is less than 0.01, while for $JT = 8$ it is about one order of magnitude larger. Differences between the representations given by the various truncations levels also emerge in power law fits such as $\overline{E(t)} \propto T_E^\gamma$. In the regime where the Hadley equilibrium is attracting, this fit is exact, with exponent $\gamma = 2$. For $T_E - T_E^{crit} \lesssim 1.5$ and $T_E > T_E^H$ (the value of the first Hopf bifurcation, see Table III), for all the values of

JT the power law fit is good, with $\gamma = 1.9 \pm 0.03$, so that a weakly subquadratic growth is realized. For $T_E - T_E^{crit} \gtrsim 1.5$, only the $JT = 32$ and 64 simulations of $\overline{E(t)}$ obey with excellent approximation a weaker power law, with $\gamma = 1.52 \pm 0.02$ in both cases, while the cases $JT = 8$ and 16 do not satisfactorily fit any power law.

The agreement worsens in the upper range of T_E, which points at the criticality of the truncation level when strong forcings are imposed. Nevertheless, the observed differences are strikingly small between the cases, say, $JT = 8$ and $JT = 64$, with respect to what could be guessed by looking at the Lyapunov dimension, entropy production, and bounding box volume diagnostics analyzed in the previous sections, where essentially only $JT = 32$ and $JT = 64$ had a satisfactory agreement. This suggests that when analyzing global observables, the resolution requirements for obtaining good statistical indicators are much more relaxed.

B. Zonal wind

We here examine the latitudinal average, denoted by $\langle \bullet \rangle$, of U and m:

$$\langle U(y,t) \rangle = \frac{1}{L} \int_0^L U(y,t) dy = \frac{2}{\pi} \sum_{j=1,\, j \text{ odd}}^{JT} \frac{U^j}{j}, \tag{81}$$

$$\langle m(y,t) \rangle = \frac{1}{L} \int_0^L m(y,t) dz = \frac{2}{\pi} \sum_{j=1,\, j \text{ odd}}^{JT} \frac{m^j}{j}. \tag{82}$$

Since $U(y,t)$ represents the zonal average of the mean of the zonal wind at the two pressure levels p_1 and p_3 at latitude y, $\langle U(y,t) \rangle$ is proportional to the total zonal momentum of the atmosphere. Instead, $\langle m(y,t) \rangle$ represents the spatially averaged halved difference between the the zonal wind at the two pressure levels p_1 and p_3. Computation of such space averages at the time-independent Hadley equilibrium (70) is straightforward:

$$\langle m\,(y) \rangle = \langle U\,(y) \rangle = \frac{R}{f_0 L_y} \frac{T_E}{2} \frac{1}{1 + \frac{\kappa}{\nu_N} \left(\frac{\pi}{L_y} \right)^2}. \tag{83}$$

Since we cannot have net, long-term zonal forces acting on the atmosphere at the surface interface, the spatial average of the zonal wind at the pressure level p_3 must be zero. Therefore, the outputs of the numerical integrations must satisfy the following constraint:

$$\overline{\langle m\,(y,t) \rangle} = \overline{\langle U\,(y,t) \rangle}, \tag{84}$$

where $\overline{X}$ denotes the time-average of the field X. The constraint (84) is automatically satisfied at the Hadley equilibrium.

The results are presented in Fig. 13. In the left panel we plot the outputs for $JT = 64$, which, similarly to the total energy case, is well representative of all the JT cases. We first note that the constraint (84) is obeyed within numerical precision. The average winds are monotonically increasing with T_E, but, when the system enters the chaotic regimes, the averages $\overline{\langle m(y,t)\rangle} = \overline{\langle U(y,t)\rangle}$ have a much smaller value than at the Hadley equilibrium, and they display sublinear growth with T_E. Moreover, for $T_E > T_E^{crit}$ the temporal variability of the time series $\langle m(y,t)\rangle$ and $\langle U(y,t)\rangle$ increases with T_E. The variability of $\langle m(y,t)\rangle$ results to be slightly larger than that of $\langle U(y,t)\rangle$, probably because the latter is related to a *bulk* mechanical property of the system such as the total zonal momentum.

Since we are dealing with a quasi-geostrophic system, these observations on the wind fields imply that while the time-averaged meridional temperature difference between the northern and southern boundary of the system increases monotonically with T_E, as to be expected, the realized value is greatly reduced by the onset of the chaotic regime with respect to the corresponding Hadley equilibrium. This is the signature of the negative feedback due to a mechanism similar to the baroclinic adjustment [66]: when the poleward eddy transport of heat is realized, it causes the reduction of the meridional temperature gradient, thus limiting the wind shear. Note that in this model the adjustment, as opposed to the general case, is essentially correct in a variational context, since only one zonal wave is considered, and so the fastest growing unstable wave is also the wave transporting northward the largest amount of heat [15, 24]. Nevertheless, the adjustment mechanism does not keep the system *close to marginal stability*, as envisioned in some baroclinic adjustment theories, since for $T_E > T_E^{crit}$ both the instantaneous and the time-averaged fields of the system are completely different from those realized at the Hadley equilibrium.

The effects of lowering JT are illustrated in Fig. 13 right. The overall agreement, expressed by a small value of the fractional differences, progressively worsens for smaller JT. Notice the similarity of the functional shapes with Fig. 12 right. The results in Fig. 13 right can be summarized as follows: the coarser-resolution models have higher total temperature difference between the two boundaries for values of T_E up to about 30 and lower temperature differences for higher values of T_E. This implies that while for $T_E \lesssim 30$ the latitudinal heat transport increases with JT as a positive trade-off between the higher number of unstable baroclinic modes (within a sloppy linear thinking) or, better, smaller scale baroclinic conversion processes taking place in a higher-dimensional attractor, and the enhancement of the barotropic and viscous stabilizing effects, for $T_E \gtrsim 30$ the converse is true.

Again, differences between the various truncations levels emerge as one attempts power law fits of the form $\overline{\langle m(y,t)\rangle} = \overline{\langle U(y,t)\rangle} \propto T_E^{\gamma}$. For the Hadley equilibrium regime we have $\gamma = 1$. For $T_E \lesssim 10$ and above the first Hopf bifurcation, for all values of JT the power law fit is good, with $\gamma = 0.875 \pm 0.05$. For $T_E - T_E^{crit} \gtrsim 1.5$, only the simulations with $JT = 32$ and 64 obey a power law (with $\gamma = 0.58 \pm 0.02$) with excellent approximation, while the realizations of the $JT = 8$ and 16 cases do not fit any power law.

By examining more detailed diagnostics on the winds, such as the time-averaged latitudinal profiles of $U(y)$ and of $m(y)$ (Fig. 14), relevant differences are observed between $JT = 8$ and the other three cases. Results are presented for $JT = 8$ and $JT = 32$, the latter being representative also of $JT = 16$ and 64. We first note that already for $T_E = 9$ and 10, such that only a weakly chaotic motion is realized, the $\overline{U(y)}$ and $\overline{m(y)}$ profiles feature in both resolutions relevant qualitative differences with respect to the corresponding Hadley equilibrium profile, although symmetry with respect to the center of the channel is obeyed. The $\overline{U(y)}$ and $\overline{m(y)}$ profiles are different (the constraint (84) being still satisfied), with $\overline{U(y)} > \overline{m(y)}$ at the center and $\overline{U(y)} < \overline{m(y)}$ at the boundaries of the channel. Nevertheless, like for the Hadley equilibrium, both $\overline{U(y)}$ and $\overline{m(y)}$ are positive and are larger at the center of the channel than at the boundaries. Consequently, at pressure level p_1 there is a westerly flow at the center of the channel and easterly flows at the two boundaries, and that at pressure level p_3 the wind is everywhere westerly and peaks at the center of the channel. Such features are more pronounced for the $JT = 32$ case, where the mechanism of the convergence of zonal momentum is more accurately represented.

For larger values of T_E, the differences between the two truncation levels become more apparent. For $JT = 8$, the observed $\overline{U(y)}$ and $\overline{m(y)}$ profiles tend to flatten in the center of the channel and to become more similar to each other. Therefore, somewhat similarly to the Hadley equilibrium case, the winds at the pressure level p_1 tend to vanish and all the dynamics is restricted to the pressure level p_3. The $\overline{m(y)}$ profiles for $JT = 32$ are quite similar to those of $JT = 8$, even if they peak and reach higher values in the center of the channel and are somewhat smaller at the boundaries. So when a finer resolution is used, a stronger temperature gradient is realized in the channel center. The $\overline{U(y)}$ profiles obtained for $JT = 32$ are instead very different. They feature a strong, well-defined peak in the channel center and negative values near the boundaries. Therefore, the winds in the upper pressure level are strong westerlies, and peak in the center of the channel, while the winds in the lower pressure level feature a relatively strong westerly jet in the center of the channel and two compensating easterly jets at the boundaries. The fact that for higher resolution the wind profiles are less smooth and have more evident jet-like features is related to the

more efficient mechanism of barotropic stabilization, which, through zonal wind convergence, *keeps the jet together* [37–40].

Examination of the latitudinal profiles in Fig. 14 clarifies our choice to extend the latitudinal domain of the model beyond the geometrically and geographically realistic mid-latitude channel. Thanks to this, the wind fields in the central portion of the domain (the latter corresponds to mid-latitudes and is of primary interest in this work), are rather different than at the boundary regions. The observed features, and especially the presence of a jet, are in qualitative agreement with the real atmosphere if models having truncation order of $JT \geq 16$ are used.

Summarizing, by considering the latitudinal average of the wind fields in the mid-latitudes range $[0.25L_y, 0.75L_y]$, the $JT = 8$ model greatly differs from the higher resolution models, since $\langle m \rangle$ and especially $\langle U \rangle$ are underestimated. Indeed, these diagnostics do not only rely on a global balance, which is relatively weakly resolution-dependent (see previous section), but also on the resolution-sensitive representation of internal processes such as the zonal wind convergence.

V. SUMMARY AND CONCLUSIONS

We have described the construction and the dynamical behavior of an intermediate complexity model of the atmospheric system. The *ab-initio* equations of dynamics and thermodynamics of a stratified fluid are specialized to the quasi-geostrophic motion and a new detailed derivation of the quasi-geostrophic two-layer model of the planetary scale atmospheric flow in a mid-latitudes beta-plane is provided. The derivation is performed by retaining, at each step, the variables as expressed in physical units, while the non-dimensionalization procedure, useful for the numerical integrations, is introduced at last.

A single zonal wave solution is assumed and a partial differential equation is derived for its coefficients. By a spectral discretization in the latitudinal direction (using a Fourier half-sine expansion), the latter equation is reduced to a system of $N = 6 \times JT$ ordinary differential equations, where $JT + 1$ is the number of nodes of the (latitudinally speaking) fastest varying base function. We have considered the cases $JT = 8$, 16, 32, and 64.

By increasing the parameter T_E, corresponding to the imposed equator-to-pole temperature gradient, the system develops a strange attractor in phase space. The route leading to the formation of this strange attractor involves:

- a Hopf bifurcation at $T_E = T_E^H$ responsible for the loss of stability of the Hadley equilibrium (corresponding to corresponding to baroclinic instability), where a periodic orbit branches off;
- a Hopf bifurcation where a two-torus is created;
- a finite number of quasi-periodic period doublings of the invariant two-torus;
- two-torus breakdown at $T_E = T_E^{crit}$.

Statistical indicators, such as lagged autocorrelations, have been used to characterize the observed quasi-periodic or strange attractors for various values of T_E. To generate the required time series, a physically relevant observable has been computed, the total energy of the system. For T_E close to T_E^{crit} quasi-periodic intermittency and very weak chaoticity are detected. The corresponding flow pattern might be classified as an amplitude vacillation, like for the two-torus dynamics. For larger T_E the lagged autocorrelation typically decays (exponentially) fast. The observed route to chaos is qualitatively the same for $JT = 16$, 32, and 64, and the values T_E^H and T_E^{crit} weakly depend on JT (Table III). Structural differences occur for $JT = 8$: a transition to a three-torus, yielding a modulated amplitude vacillation, is involved.

The strange attractor is further studied by means of the Lyapunov exponents, where we have varied both T_E and model resolution JT. Although the system qualitative behavior is analogous for different values of JT, there are significant quantitative differences. In all cases, the maximal Lyapunov exponent λ_1 increases with T_E, and it is possible to robustly fit a power law of the form $\lambda_1 \propto (T_E - T_E^{crit})^{\gamma}$. For T_E fixed, the maximal Lyapunov exponent decreases with JT (so that the predictability time increases). On the contrary, the metric entropy increases linearly with T_E for all examined values of JT, and is larger for larger values of JT. In other words, the fastest (the total) dynamical instability of the system is smaller (larger) for larger JT, where the dynamics is more accurately represented.

The Lyapunov dimension D_L increases with both T_E and JT. The dependence of D_L on T_E is qualitatively the same for all values of JT: by increasing T_E there is an initial phase where the dimension quickly grows with a power law $D_L \propto (T_E - T_E^{crit})^{\gamma}$, followed by a linear scaling regime. For large T_E, the dimension *saturates* and depends sublinearly on T_E. The latter effect is, of course, more evident for small values of JT. It provides a measure of accuracy of the spectral discretization (as far as the details of the dynamics are concerned), which turns out to depend on T_E.

When considering the bounding box of the system, *i.e.* the minimal hyperparallelepiped containing the attractor in phase space, for sufficiently high truncation order JT each side of the box increases as $\propto (T_E - T_E^{crit})^{1/3}$ for $T_E - T_E^{crit} \lesssim 1.5$ and as $\propto (T_E - T_E^{crit})^{5/6}$ for larger values of T_E. So for a given value of JT the ratios of the ranges of the various degrees of freedom remain essentially unchanged when varying T_E, yielding a self-similar scaling property. The volume of the bounding box V_{BB} then results to increase as $\propto (T_E - T_E^{crit})^{N/3}$ and as $\propto (T_E - T_E^{crit})^{5N/6}$ in the mentioned domains of T_E.

A peculiar feature of this dynamical system is the rather smooth dependence on the parameter T_E of all the examined properties of the strange attractor. No windows of periodicity have been detected in the chaotic range and this is quite uncommon especially when comparing with low-dimensional chaotic systems such as the Hénon-Pomeau mapping [51, 52] or the Lorenz flow [19] (also see [30, 44, 49]). Although *structural stability* [30] is out of the question, other stability concepts (such as robustness [55]) might provide an alternative and more practical theoretical basis for the explanation of the observed parametric smoothness, perhaps also for other systems of intermediate and high dimensionality.

Despite the sensitivity of Lyapunov exponents and dimension to model resolution JT, certain observables of physical interest, such as the time-averaged total energy of the system, or the time-averaged spatially averaged zonal wind fields, are in *quantitative* agreement for all values of JT, except for high values of T_E. Indeed these quantities are representative of

global balances, which turn out to be only slightly affected by model resolution. When the system enters the chaotic regime, the average total energy and average zonal winds have lower values than those of the coexisting - and unstable - Hadley equilibrium, because the chaos-driven occupation of the faster-varying latitudinal modes fuels viscous dissipation, which acts preferentially on the small scales. Other mechanisms which are present in the real atmosphere, such as the *barotropic governor* [65], are not represented in this schematic model. Moreover, the total energy and the average wind field at the Hadley equilibrium depend quadratically and linearly on T_E, respectively, in the chaotic regimes such quantities obey a subquadratic and sublinear power law $\propto T_E^{\gamma}$, respectively. For both quantities, the exponents of the power laws decrease abruptly as $T_E - T_E^{crit}$ crosses 1.5. An analogous sharp change is observed for V_{BB}, which suggests the onset of a self-similar scaling law.

Nevertheless, when analyzing more detailed diagnostics on the winds at the two pressure levels, relevant differences emerge between the model with $JT = 8$ and those with the higher resolutions. For $JT = 8$ the wind profiles are rather flat in latitude and very weak in the lower pressure level. For the higher resolution models the winds in the upper pressure level are strong westerlies and peak in the center of the channel (corresponding to mid-latitudes), in qualitative agreement with reality. The winds in the lower pressure level feature a relatively strong westerly jet in the center of the channel and two compensating easterly jets at the boundaries. The fact that for higher resolution the wind profiles are less smooth and have more clear-cut jet-like features is related to the more efficient mechanism of barotropic stabilization, which, through zonal wind convergence, *keeps the jet together*.

The model we study, although admittedly very schematic, is Earth-like in that it features some fundamental processes determining the general circulation of the Earth atmosphere, in particular:

- the complex process of atmospheric baroclinic conversion, transforming available potential energy associated with (latitudinally) differential Sun heating into kinetic energy of synoptic scale motions of the mid-latitudes atmosphere;
- nonlinear stabilization by eddy momentum convergence from non-symmetric baroclinic disturbances into the zonal jet;
- viscous dissipation.

While the baroclinic conversion process is essentially well represented in all models (even if those with higher resolution are more efficient in the conversion for large T_E, since conversion can take place also on smaller spatial scales), the descriptions of the barotropic zonal

wind convergence and of the viscous dissipation are much more critically dependent on the latitudinal truncation order, since the latter processes are represented by terms involving the latitudinal derivatives of the fields.

When a larger pool of available energy is provided, the dynamics of the system is richer, since the baroclinic conversion process can transfer larger amounts of energy to the disturbances: for each given value of JT, the largest Lyapunov exponent, the metric entropy, the Lyapunov dimension of the attractor, the mean and the variability of the total energy and of the latitudinally averaged zonal wind fields all increase with T_E. The enhancement of the efficacy of the baroclinic conversion process when higher resolution is adopted is highlighted by the increase with JT, for a fixed value of T_E, of the number of linearly unstable modes of the Hadley equilibrium, of the Lyapunov dimension of the attractor, and of the metric entropy.

The critical dependence of the efficiency of the two mentioned stabilizing processes on the model resolution is illustrated by several results, *e.g.* in the dependence of the parameters T_E^H and T_E^{crit} on JT (it is easier to destabilize a system with lower resolution), in the fact that there are fewer unstable modes of the Hadley equilibrium for larger values of JT in the vicinity of T_E^H, in the fact that the predictability time increases with JT for a given value of T_E and in the features of the latitudinal profiles of the winds.

Although relevant ingredients of geometrical (horizontal convergence due to the Earth curvature, latitudinal boundary conditions at the margins of the middle latitude circumpolar vortex, etc.) and dynamical (stabilization mechanisms other then momentum convergence such as the so-called *barotropic governor* [65]) nature of the real atmospheric circulation are still missing in this, very preliminary, theoretical representation, some important general conclusions are drawn from the described results.

Pessimistic conclusions (in increasing order of pessimism):

- No simple *mean field* or *macroscopic adjustment* theory can be formulated for such complex nonlinear systems, even for relatively simple models as those proposed in this work.

- It is, in general, doubtful whether *invariant manifolds* in phase space - such as fixed points, periodic orbits - carry any useful information concerning the general circulation of the system.

- Beyond the time of deterministic predictability, "averaging" is of no practical use; it is not clear what else should be done in order to produce *useful* - in a statistical sense - *predictions*.

Optimistic conclusions:

- Although some dynamical system properties, such as Lyapunov exponents and dimension, are strongly model-dependent, some other - of great physical interest - are not.
- Increasing refinement (number of degrees of freedom) of models may produce smoother dependence on macroscopic parameters.
- It is not outside the range of practically feasible, although possibly challenging, projects to put together an intermediate dimensionality model - with hundreds of (well chosen!) degrees of freedom - with *stable properties* which is relevant for a theory of general atmospheric circulation.

Acknowledgments

We wish to thank Mara Felici for technical and scientific help.

APPENDIX A: ON THE NUMERICAL METHODS

We begin by describing the projection operator used in the definition of the vector field (61)-(66). As it is customary with climatological spectral models [32], a pseudospectral method is used, also known as Fourier collocation [64, 67].

The fields A, B, U, m, appearing in the nonlinear terms of (61)-(66), are first evaluated at JT collocation points $y_1, \ldots, y_{JT}$, equally spaced in the y-domain $(0, L_y)$. This is achieved by a Discrete Sine Transform of A_j^1, A_j^2, B_j^1, B_j^2, U_j, m_j, with $j = 1, \ldots, JT$. The terms involving second derivatives with respect to y are also computed in this way, by premultiplying for a suitable coefficient involving the wave numbers w_j. Then all the nonlinear terms are evaluated pointwise, at each of the collocation points $y_1, \ldots, y_{JT}$. Lastly, an inverse Discrete Sine Transform is carried out, yielding the Fourier coefficients of the nonlinear terms. The software library `fftw3` [68], publicly available at `www.fftw.org`, has been used for the Discrete Sine Transform.

The numerical solution of the system of ordinary differential equations (61)-(66) is computed by means of a standard Runge-Kutta-Fehlberg(4,5) algorithm [69] with adaptive stepsize, where the approximated solution is carried by the order five method. The local truncation error is kept below $1.e-6$. The stepsize adjustment procedure is similar to that of `DOPRI5`, available at (`www.unige.ch/~hairer`).

The total energy of (61)-(66), is computed according to (75). In terms of the Fourier coefficients A_j^1, B_1^j, ..., this yields the expression

$$
\begin{aligned}
E(t) = L_x L_y \Bigg\{ & \left(\frac{12\pi}{L_x}\right)^2 \sum_{j=1}^{JT} \left(\left(A_j^1\right)^2 + \left(B_j^1\right)^2 + \left(\frac{\pi}{L_y}\right)^2 j^2 \left(\left(A_j^2\right)^2 + \left(B_j^2\right)^2 \right) + \frac{2}{H_2^2} \left(B_j^2\right)^2 \right) + \\
& \left(\frac{12\pi}{L_x}\right)^2 \sum_{j=1}^{JT} \left(\left(A_j^2\right)^2 + \left(B_j^2\right)^2 + \left(\frac{\pi}{L_y}\right)^2 j^2 \left(\left(A_j^1\right)^2 + \left(B_j^1\right)^2 \right) + \frac{2}{H_2^2} \left(B_j^1\right)^2 \right) + \\
& \frac{1}{2} \sum_{j=1}^{JT} \left(U_j^2 + m_j^2 + \frac{2}{H_2^2} \left(\frac{L_y}{\pi}\right)^2 \left(\frac{m_j}{j}\right)^2 \right) \Bigg\}.
\end{aligned}
\tag{A1}
$$

For the computation of the averages in Sec. IV, time series of 315360 adimensional time units (1000 years in natural units) have been computed for all values of JT, preceded by a transient of five years (time is expressed in the scale of the system, see Table I). The observables $E(t)$, $U(y,t)$, and $m(y,t)$ have been sampled every 0.216 time units (four times a day), thereby obtaining time series of 1460000 elements. The sample mean and sample

standard deviation have been computed according to the usual formulas:

$$\overline{E(t)} = \frac{1}{n}\sum_{i=1}^{n} E(t_i), \qquad \sigma_E^2 = \frac{1}{n-1}\left(\sum_{i=1}^{n} E^2(t_i) - n\overline{E(t)}^2\right). \tag{A2}$$

The initial condition used for all computations is $A_1^1 = -0.8, A_2^1 = 0.65, B_1^1 = 0.2, B_2^1 = 0.2, B_1^2 = 0.4, B_2^2 = 0.1, U_1 = 1.26, m_1 = 1.1$, with the remaining coefficients set to 0, as in [24].

APPENDIX B: LYAPUNOV EXPONENTS

The Lyapunov exponents of system (61)-(66) are estimated according to the algorithm described by Galgani, Giorgilli, Benettin and Strelcyn [70]. The first variational equations of (61)-(66) are integrated during a period of time T, with the identity matrix as initial condition. During integration, at time t the canonical orthonormal basis is mapped onto a new set of vectors $(\mathbf{v}_1^t, \mathbf{v}_2^t, \ldots, \mathbf{v}_N^t)$, where $N = 6 \times JT$ is the dimension of the phase space. Each vector tends to align itself along the direction of maximal expansion (or of minimal compression). Thus all $\mathbf{v}_j^t$'s tend to collapse onto one direction. To prevent this, the Gram-Schmidt process is applied to $(\mathbf{v}_1^{t_1}, \mathbf{v}_2^{t_1}, \ldots, \mathbf{v}_N^{t_1})$ at $t = t_1$, yielding a set $(\tilde{\mathbf{v}}_1^{t_1}, \ldots, \tilde{\mathbf{v}}_N^{t_1})$ of orthogonal vectors. The vectors are normalized by putting $\mathbf{w}_j^{t_1} = \tilde{\mathbf{v}}_j^{t_1} / \|\tilde{\mathbf{v}}_j^{t_1}\|$ for $j = 1, \ldots, N$. Then a new frame of vectors $(\mathbf{v}_1^{t_2}, \ldots, \mathbf{v}_N^{t_2})$, with $t_2 = 2t_1$, is computed by integrating the first variational equations taking as initial condition the orthonormal vectors $(\mathbf{w}_1^1, \ldots, \mathbf{w}_N^1)$ from the previous step, and the whole process is repeated. At iteration step k, define $t_k = kt_1$ and

$$c_j^k = \prod_{i=1}^{k} \|\tilde{\mathbf{v}}_j^{t_k}\| \quad \text{and} \quad \mathbf{w}_j^{t_k} = \frac{\tilde{\mathbf{v}}_j^{t_k}}{\|\tilde{\mathbf{v}}_j^{t_k}\|} \quad \text{for} \quad j = 1, \ldots, N.$$

The orthonormalization process does not change the direction of $\mathbf{v}_1^{t_k}$, so that $\mathbf{w}_1^{t_k}$ still points to the direction of maximal stretch. Denoting by λ_j, $j = 1, \ldots, N$, the Lyapunov exponents in decreasing order of magnitude, the length c_1^k of $\mathbf{v}_1^{t_k}$ is approximately proportional to $e^{k\lambda_1}$. The plane spanned by $\mathbf{v}_1^{t_k}$ and $\mathbf{v}_2^{t_k}$ is not changed by the Gram-Schmidt process and tends to adjust to the subspace of maximal growth of surfaces. The rate of growth of areas is proportional to $e^{k(\lambda_1+\lambda_2)}$. In particular, since $\mathbf{v}_1^{t_k} = \mathbf{w}_1^{t_k}$ and $\mathbf{w}_2^{t_k}$ are orthonormal, the length of the projection of $\mathbf{v}_2^{t_k}$ upon $\mathbf{w}_2^{t_k}$ is proportional to $e^{k\lambda_2}$. A similar argument for growth of volumes yields that c_j^k is proportional to $e^{k\lambda_j}$. Therefore, the Lyapunov exponent λ_j is estimated by the averages

$$\lambda_j \approx \frac{1}{k} \log(c_j^k), \tag{B1}$$

where $k = T/t_1$. We have chosen T of the order of 3150 adimensional time units (about 10 years in natural units) for all values of JT, while t_1 has been chosen as 0.864 adimensional time units (1 day), which allow for an excellent convergence of the exponents.

Actually, we have used a version of the algorithm [70] in which the variational equations are not integrated explicitly, but approximated by means of numerical differentiation: N trajectories are simultaneously integrated, starting from points nearby a reference orbit. The distances from the reference orbit are normalized at regular time steps [71].

The library `LAPACK` (`www.netlib.org`) has been used for Gram-Schmidt orthogonaliza-

tion and for other computations in this work.

Variable	Scaling factor	Value of scaling factor
x	l	$10^6 m$
y	l	$10^6 m$
t	$u^{-1}l$	$10^5 s$
ψ_1	ul	$10^7 m^2 s^{-1}$
ψ_3	ul	$10^7 m^2 s^{-1}$
ϕ	ul	$10^7 m^2 s^{-1}$
τ	ul	$10^7 m^2 s^{-1}$
A_n^1	ul	$10^7 m^2 s^{-1}$
B_n^1	ul	$10^7 m^2 s^{-1}$
A_n^2	ul	$10^7 m^2 s^{-1}$
B_n^2	ul	$10^7 m^2 s^{-1}$
m	u	$10 m s^{-1}$
U	u	$10 m s^{-1}$
m_n	u	$10 m s^{-1}$
U_n	u	$10 m s^{-1}$
w_n	l^{-1}	$10^{-6} m^{-1}$
Lag	$u^{-1}l$	$10^5 s$
λ_j	ul^{-1}	$10^{-5} s^{-1}$
t_p	$u^{-1}l$	$10^5 s$
T	$ulf_0 R^{-1}$	$3.5K$
E	$u^2 l^2 (\delta p) g^{-1}$	$5.1 \times 10^{17} J$

TABLE I: Variables of the system and non-dimensionalization factors. For A_n^1, B_n^1, A_n^2, B_n^2, m_n, U_n, and w_n, the index n ranges from 1 to JT. For λ_j, $n = 1, \ldots, 6 \times JT$.

Parameter	Dimensional Value	Non-dimensional value	Scaling factor	Value of scaling factor
L_x	$3 \times 10^7 m$	29	l	$10^6 m$
L_y	$10^7 m$	10	l	$10^6 m$
χ	$2\pi/\left(4.833 \times 10^6\right) m^{-1}$	1.3	l^{-1}	$10^{-6} m^{-1}$
H_2	$7.07 \times 10^5 m$	7.07×10^{-1}	l	$10^6 m$
f_0	$10^{-4} s^{-1}$	10	ul^{-1}	$10^{-5} s^{-1}$
β	$1.6 \times 10^{-11} m^{-1} s^{-1}$	1.6	ul^{-2}	$10^{-11} m^{-1} s^{-1}$
ν_E	$5.5 \times 10^5 m^2 s^{-1}$	5.5×10^{-2}	ul	$10^7 m^2 s^{-1}$
κ	$2.8 \times 10^5 m^2 s^{-1}$	2.8×10^{-2}	ul	$10^7 m^2 s^{-1}$
ν_N	$1.1 \times 10^{-6} s^{-1}$	1.1×10^{-1}	ul^{-1}	$10^{-5} s^{-1}$
T_E	$28K$ to $385K$	8 to 110	$ulf_0 R^{-1}$	$3.5K$

TABLE II: Values of the parameters used in this work and non-dimensionalization factors.

JT	T_E^H	T_E^{crit}
8	7.83	9.148
16	8.08	8.415
32	8.28	8.522
64	8.51	8.663

TABLE III: Approximate values of the parameter T_E where the Hadley equilibrium loses stability via Hopf bifurcation (T_E^H) and where the onset of the chaotic regime occurs (T_E^{crit}) for each of the considered orders of truncation JT. See text for details.

JT	$\gamma[\log(T_E - T_E^{crit}) \leq 0.5]$	$\gamma[\log(T_E - T_E^{crit}) \geq 0.5]$
8	40 ± 1	40 ± 1
16	33 ± 3	80 ± 1
32	66 ± 2	160 ± 1
64	133 ± 4	320 ± 1

TABLE IV: Power-law fits of the volume of the bounding box as $V_{BB} \propto (T_E - T_E^{crit})^\gamma$ in two different ranges of $T_E - T_E^{crit}$ for each of the considered orders of truncation JT. See text and Fig. 11 for details.

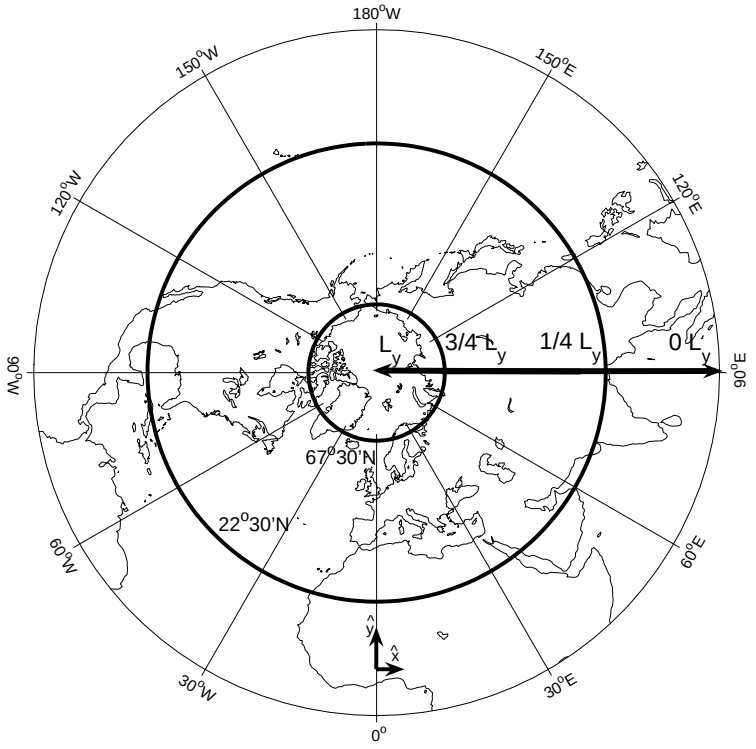

FIG. 1: Sketch of the actual geographical area corresponding to the simplified β channel. The local x and y directions and the β-channel width L_y are indicated. The mid-latitudes range from $1/4L_y$ to $3/4L_y$, corresponding to a 45^o latitudinal belt centered at 45^oN.

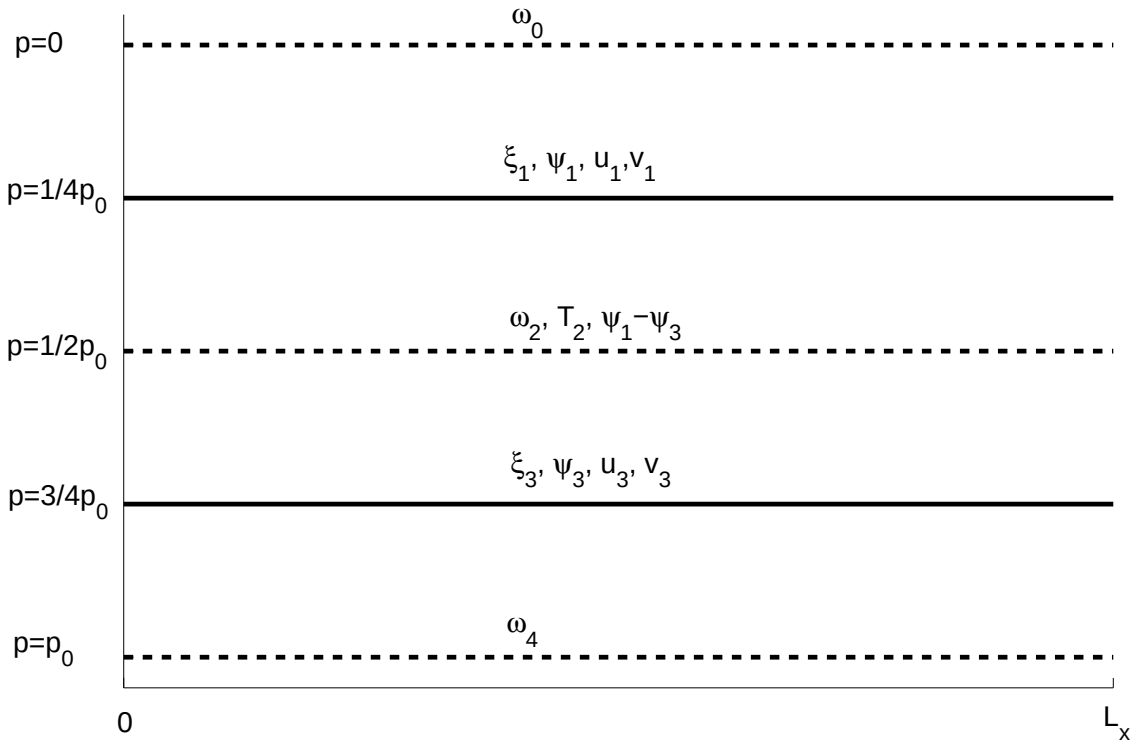

FIG. 2: Sketch of the vertical-longitudinal section of the system domain. The domain is periodic in the zonal direction x with wavelength L_x. At each pressure level, the relevant variables are indicated.

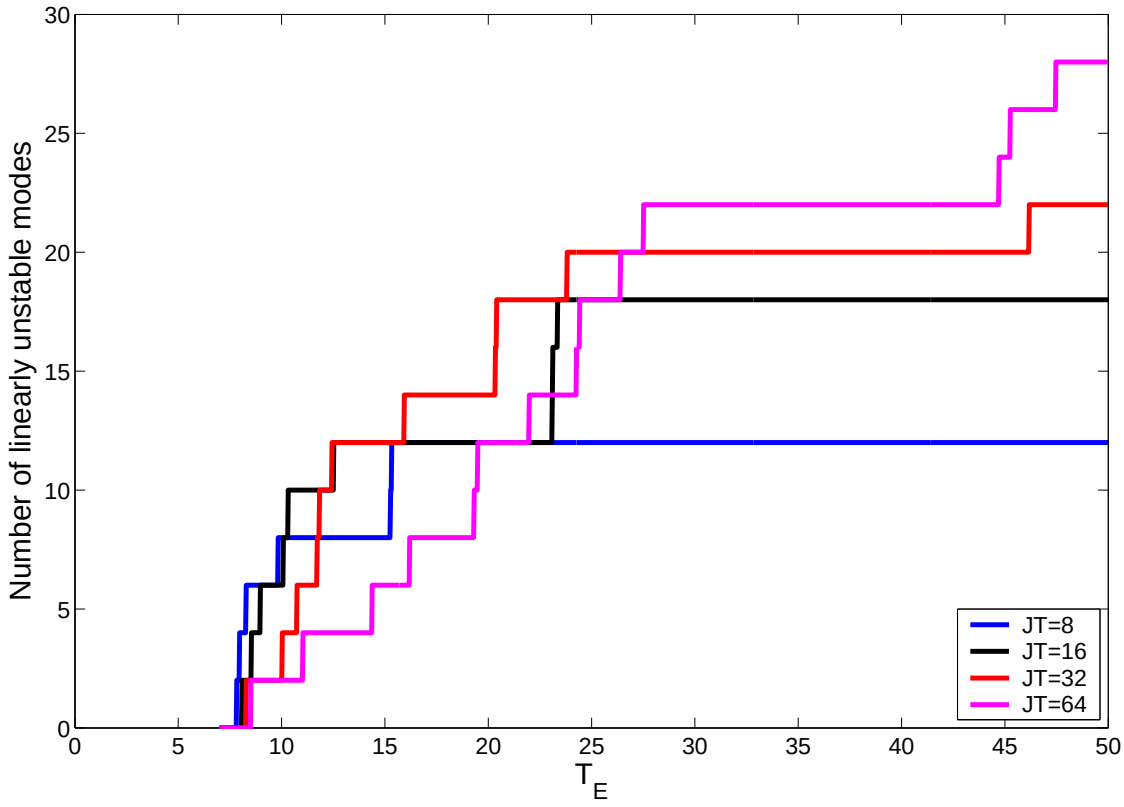

FIG. 3: Number of linearly unstable modes at the Hadley equilibrium as a function of the parameter T_E for $JT = 8$, 16, 32, 64.

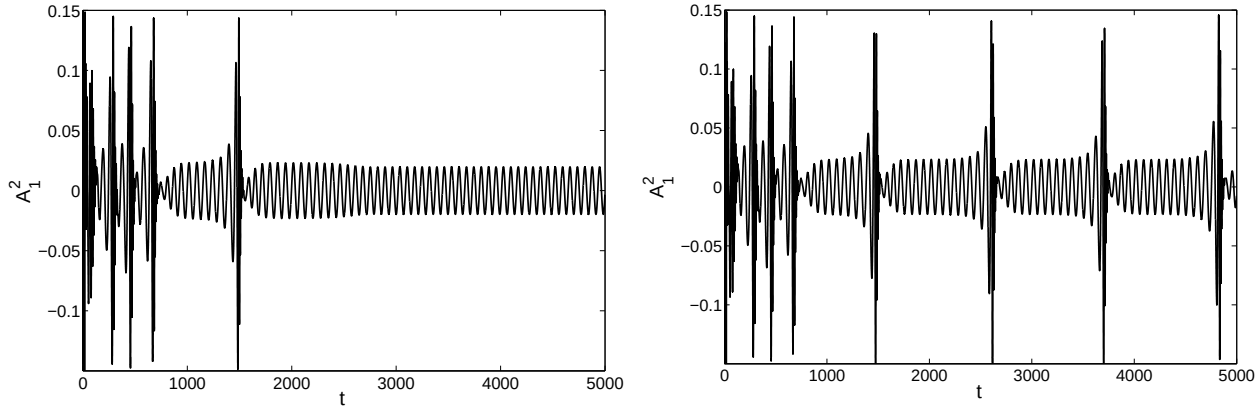

FIG. 4: Time-evolution of the component A_1^2 of system (61)-(66), starting from the initial condition mentioned in Appendix A. Left: $T_E = 8.484631$. Right: $T_E = 8.484632$. No transient has been discarded.

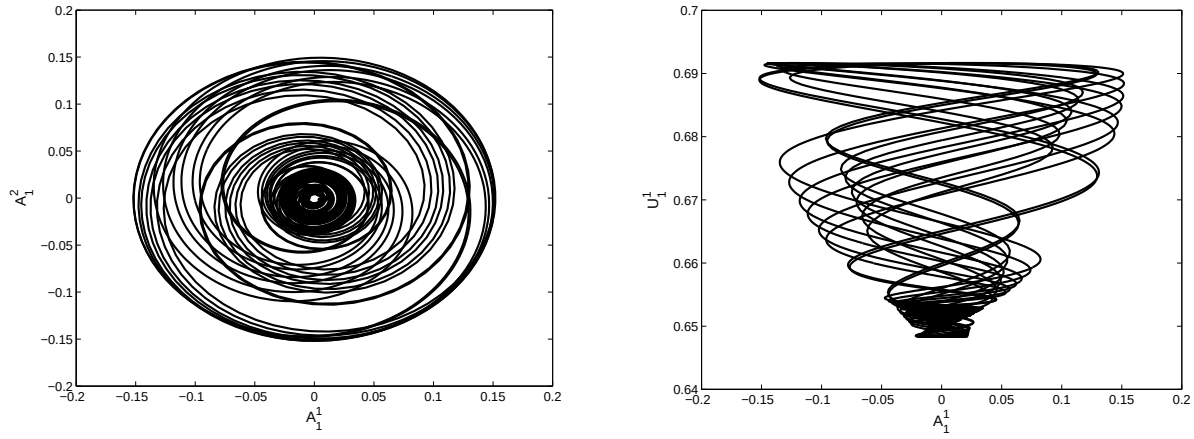

FIG. 5: Left: projection on (A_1^1, A_1^2) of an orbit on the attracting two-torus of (61)-(66) for $T_E = 8.484632$. Right: same as Left, projection on (A_1^1, U_1^1). Units as indicated in Table I. A five-year transient has been discarded. The phase-space region where the orbit accumulates more densely is due to intermittency of saddle-node type near the location of the periodic orbit occurring for $T_E = 8.484631$, compare Fig. 4 and see text for details.

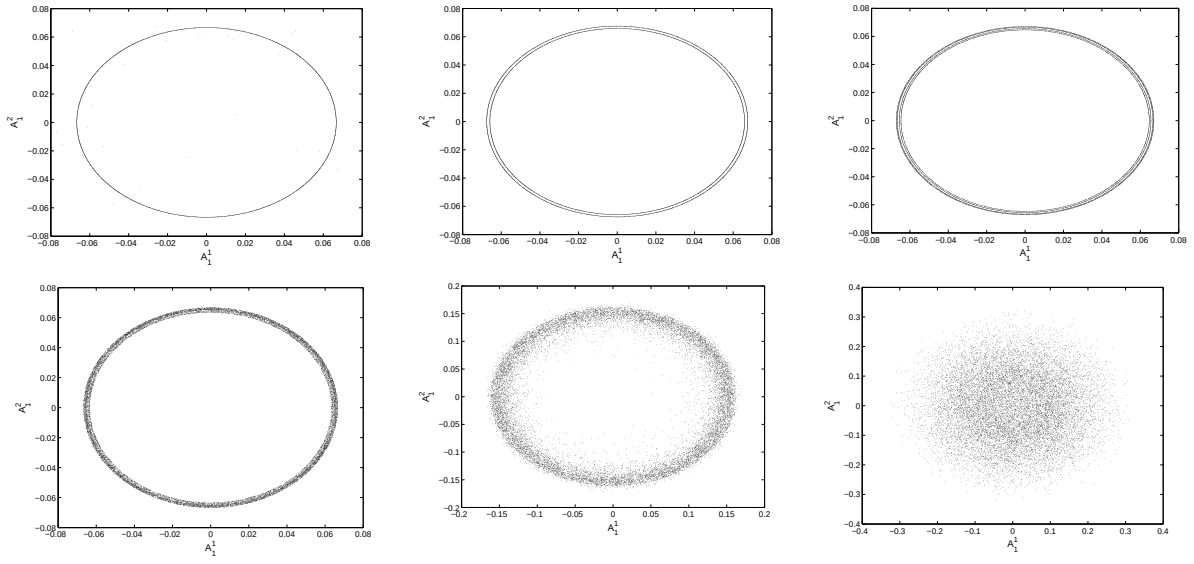

FIG. 6: Projections on (A_1^1, A_1^2) of a Poincaré section of the attractor of (61)-(66), obtained by intersecting it with a hyperplane $U_1 = c_0$ for several values of T_E. From (A) to (F) T_E is, respectively, 8.516, 8.52, 8.521, 8.522, 8.58, 10. The value c_0 of the section is fixed at 0.66 (A) to (D) and is 0.7 and 0.8 for (E) and (F) respectively. Also notice the different axis scale for the last two plots.

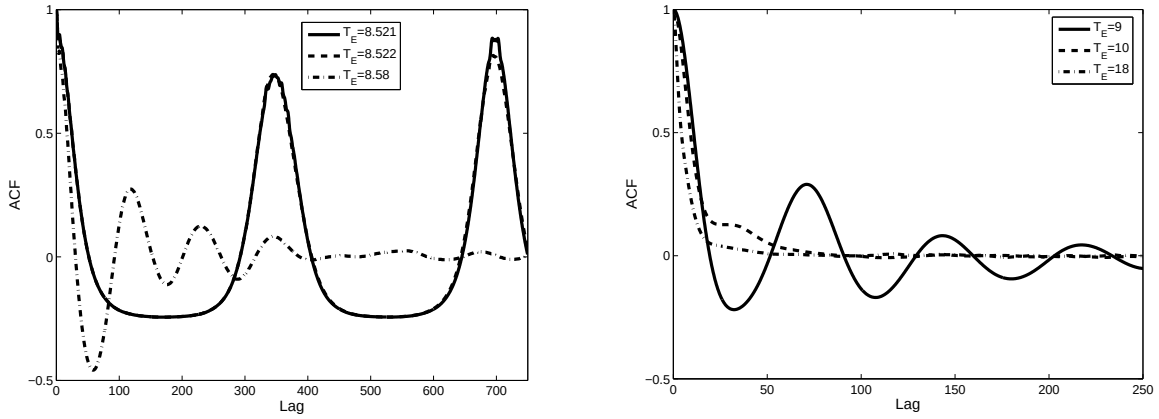

FIG. 7: Autocorrelations of the total energy time series on the attractor of (61)-(66), for various values of T_E. Left: $T_E = 8.521$, 8.522, 8.58; Right: $T_E = 9$, 10, 18.

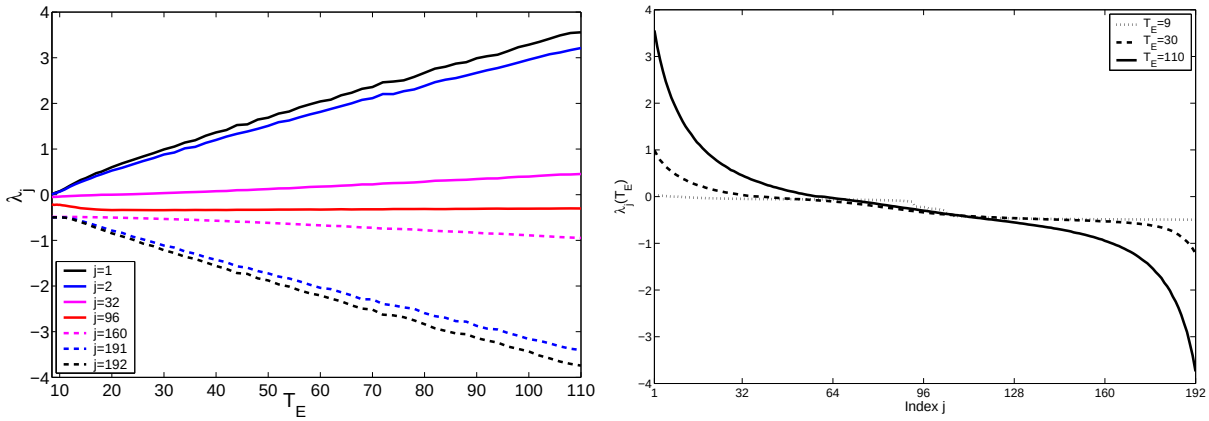

FIG. 8: Left: Lyapunov exponents λ_j for $JT = 32$ and for $j = 1$, 2, 32, 96, 160, 191, 192 as a function of T_E. Right: Spectrum of the Lyapunov exponents for $T_E = 9$, $T_E = 30$, and $T_E = 110$. Units as for λ_j and T_E as described in Table I.

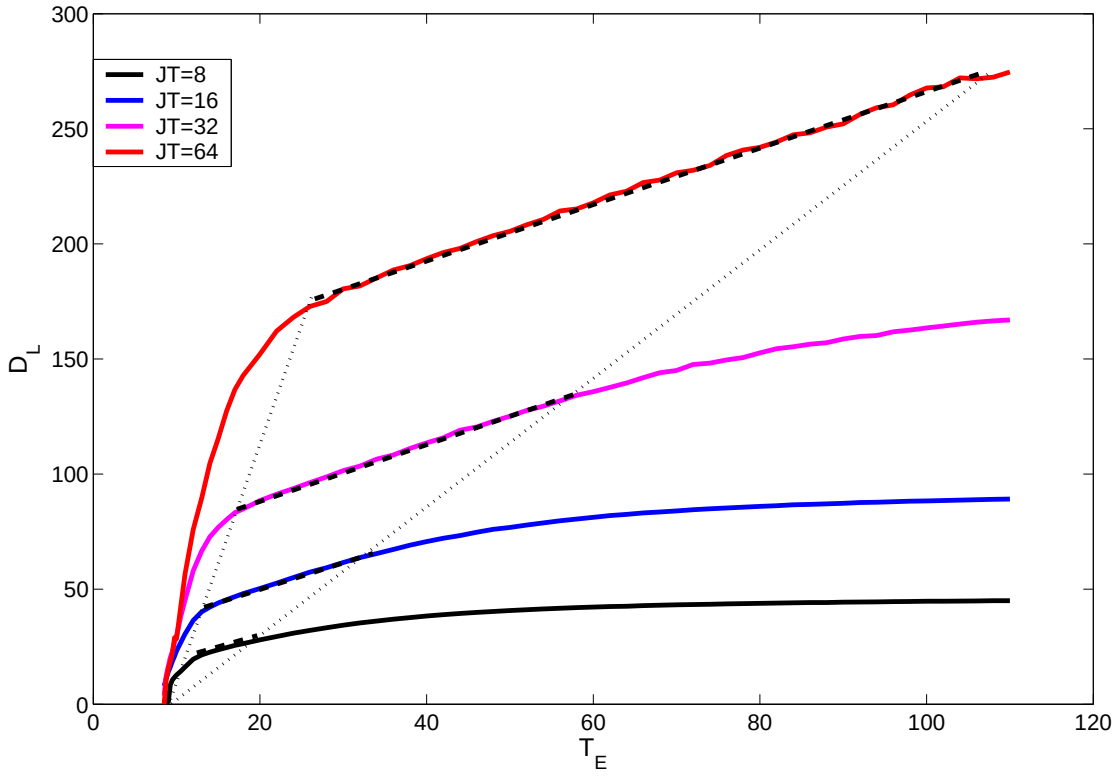

FIG. 9: Lyapunov dimension of the attractor of (61)-(66) as a function of T_E for $JT = 8$, 16, 32, and 64. All the straight lines are parallel and the domain of validity of the linear fit is apparently homothetic.

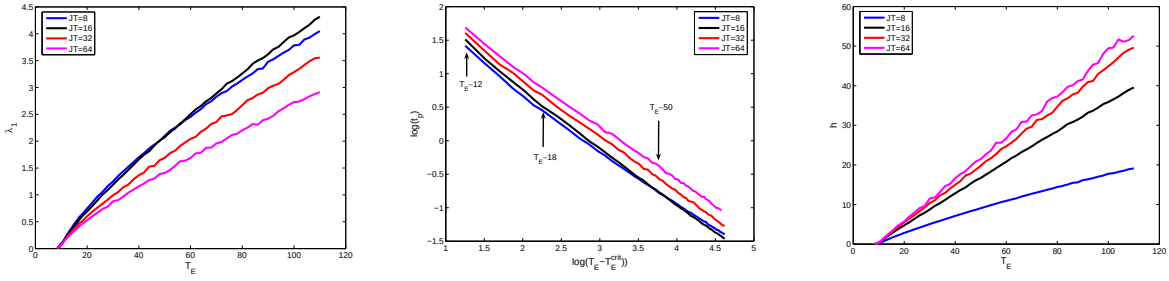

FIG. 10: Left: maximal Lyapunov exponent on the attractor of (61)-(66) as a function of T_E for $JT = 8$, 16, 32, 64. Center: Log-Log plot of the predictability time of the system $t_p = \lambda_1^{-1}$ versus $T_E - T_E^{crit}$. Power laws ($t_p \propto (T_E - T_E^{crit})^\gamma$) are detected for all considered values of JT. Right: metric entropy. Linear dependences $h \sim \beta(T_E - T_E^{crit})$ occur for all values of JT.

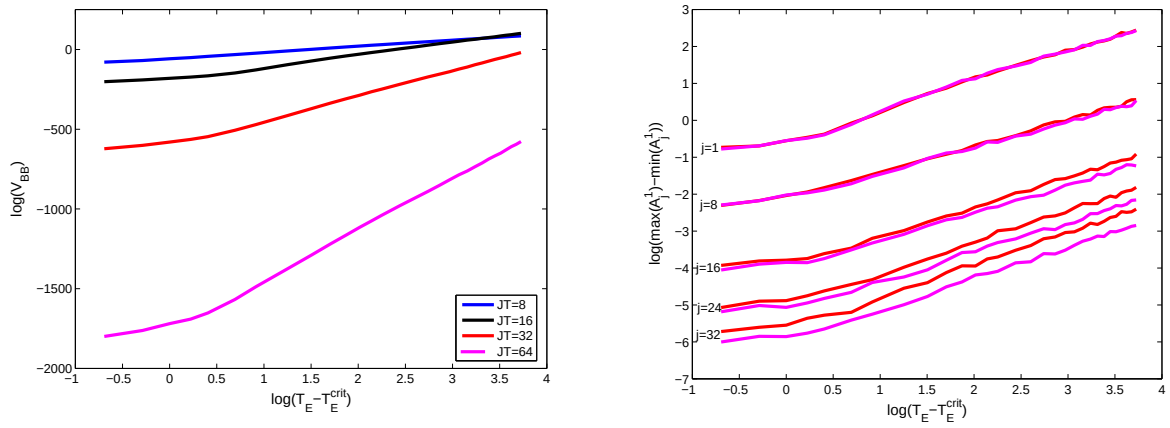

FIG. 11: Left: Volume of the bounding box V_{BB} of the attractor as a function of the detuning parameter $T_E - T_E^{crit}$ for $JT = 8$, 16, 32, 64. For description of the power law fits, see text and Table IV. Right: Value of the corresponding sides of the bounding box pertaining to the variables A_j^1 for $JT = 32$ (red lines) and 64 (magenta lines). Notice the two power-law regimes mentioned in the text.

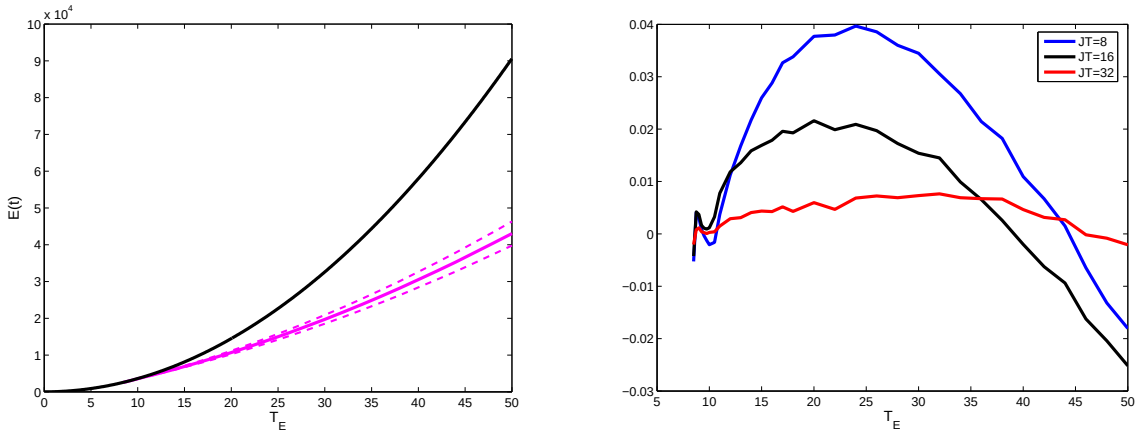

FIG. 12: Left: $\overline{E(t)}$ for the Hadley equilibrium (black line) and deduced from the observed fields in the chaotic regime for $JT = 64$ (magenta line); the magenta dashed line delimit the σ-confidence interval. Right: fractional deviations of $\overline{E(t)}$, for $JT = 8$, 16, and 32, with respect to $JT = 64$. See text for details.

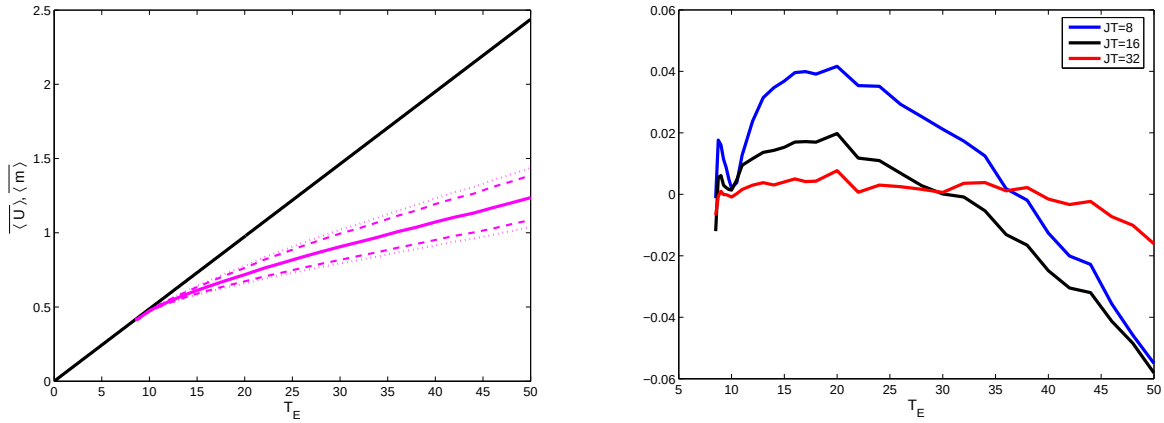

FIG. 13: Left: $\overline{\langle U \rangle} = \overline{\langle m \rangle}$ for the Hadley equilibrium (black line) and deduced from the observed fields in the chaotic regime for $JT = 64$ (magenta line); the magenta dashed and dotted lines delimit the σ-confidence interval for $\langle U \rangle$ and $\langle m \rangle$, respectively. Right: fractional deviations of $\overline{\langle U \rangle} = \overline{\langle m \rangle}$ for $JT = 8$, 16, and 32 with respect to $JT = 64$. See text for details.

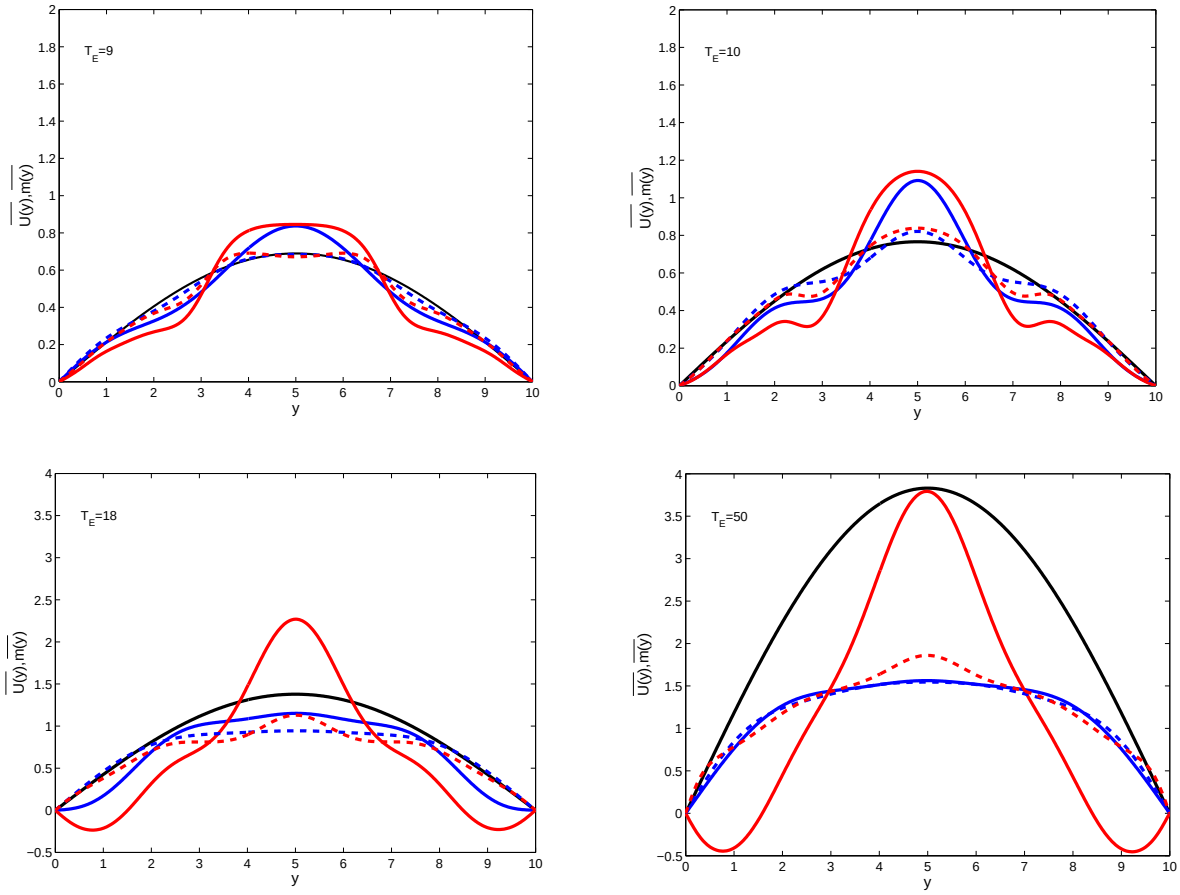

FIG. 14: Time-averaged latitudinal profiles $\overline{U(y)}$ (solid lines) and $\overline{m(y)}$ (dashed lines). In all figures the black solid line indicates the $U(y) = m(y)$ profile of the Hadley equilibrium, the blue and red lines refer to the cases $JT = 8$ and $JT = 32$, respectively. The values of T_E are indicated. Note that the vertical scale for $T_E = 9$ and 10 is about 1/2 as for the other two figures.

[1] J.P. Peixoto, A.H. Oort: *Physics of Climate*, Am. Inst. of Phys., College Park, 1992.

[2] V. Lucarini: Towards a definition of climate science, *Int. J. Environment and Pollution* **18** (2002), 409–414.

[3] E.N. Lorenz: The predictability of a flow which possesses many scales of motion, *Tellus* **21**, (1969), 289–307.

[4] E.N. Lorenz: Nondeterministic theories of climatic change, *Quaternary Res.* **6** (1976), 495–506.

[5] J.G. Charney, R. Fjörtoft, J. von Neumann: Numerical integration of the barotropic vorticity equation, *Tellus* **2** (1950), 237–254.

[6] E.N. Lorenz: *The Nature and Theory of the General Circulation of the Atmosphere*, World Meteorol. Organ., Geneva, 1967.

[7] E.N. Lorenz: A History of Prevailing Ideas about the General Circulation of the Atmosphere, *Bull. Am. Met. Soc.* **64** (1983), 730–769.

[8] H. Jeffreys: On the Formation of Waves by Wind, *Proc. Roy. Soc. Lond.* **107** (1924), 189–206.

[9] H. Jeffreys: On the Formation of Waves by Wind, *Proc. Roy. Soc. Lond.*, **110A** (1925), 341–347.

[10] E. Palmen: The Role of Atmospheric Disturbances in the General Circulation, *Quart. J. Roy. Meteor. Soc.* **77** (1951), 337–354.

[11] M. Margules: Die energie der Stürme, *Jahrb. Zentralanst. Meteor. Wien* **40** (1903), 1–26.

[12] E.N. Lorenz: Available potential energy and the maintenance of the general circulation, *Tellus* **7**, (1955), 157–167.

[13] E.N. Lorenz: Generation of available potential energy and the intensity of the general circulation, in *Dynamics of Climate*, R.L. Pfeffer ed., Pergamon, Tarrytown (1960), 86–92.

[14] M.L. Blackmon: A climatological spectral study of the 500 mb geopotential height of the Northern Hemisphere, *J. Atmos. Sci.* **33** (1976), 1607–1623

[15] A. Speranza: Deterministic and statistical properties of the westerlies, *Paleogeophysics* **121** (1983), 511–562

[16] A. dell'Aquila, V. Lucarini, P.M. Ruti, S. Calmanti: Hayashi spectra of the northern hemisphere mid-latitude atmospheric variability in the NCEP–NCAR and ECMWF reanalyses, *Clim. Dyn.* (2005), DOI: 10.1007/s00382-005-0048-x.

[17] J.G. Charney: The Dynamics of Long Waves in a Baroclinic Westerly Current, *J. Atmos. Sci.* **4** (1947), 136–162.

[18] E.T. Eady: Long waves and cyclone waves, *Tellus* **1** (1949), 33–52.

[19] E.N. Lorenz: Deterministic Nonperiodic Flow, *J. Atmos. Sci.* **20** (1963), 130–141.

[20] Intergovernmental Panel on Climate Change 2001, Working Group I: *Climate Change 2001: The Scientific Basis*, Cambridge University Press, Cambridge, 2001.

[21] N.M.J. Hall, P.D. Sardeshmukh: Is the time-mean Northern Hemisphere flow baroclinically unstable?, *J. Atmos. Sci.*, **55** (1998), 41–56.

[22] H.L. Kuo: On Production of Long-term Mean Zonal Current and Eddy Momentum and Heat Transports in Atmosphere, *Pure Appl. Geophys.* **158** (2001), 1047–1064.

[23] J.D. Farmer: Chaotic attractors of an infinite-dimensional dynamic system, *Physica D* **4** (1982), 366–393.

[24] A. Speranza, P. Malguzzi: The statistical properties of a zonal jet in a baroclinic atmosphere: a semilinear approach. Part I: two-layer model atmosphere, *J. Atmos. Sci.* **48** (1988), 3046–3061.

[25] P. Malguzzi, A. Trevisan, A. Speranza: Statistics and predictability for an intermediate dimensionality model of the baroclinic jet, *Ann. Geoph.* **8** (1990), 29–35.

[26] J.S. Frederiksen: Instability theory and nonlinear evolution of blocks and mature anomalies, *Advances in Geophysics* **29** (1986), 277–303.

[27] E.N. Lorenz: Attractor sets and quasi-geostrophic equilibrium, *J. Atmos. Sci.* **37** (1980), 1685–1699.

[28] J. Pedlosky: *Geophysical Fluid Dynamics* (2nd ed.), Springer-Verlag, New York, 1987.

[29] N.A. Phillips: Energy transformations and meridional circulations associated with simple baroclinic waves in a two-level, quasi-geostrophic model, *Tellus* **6** (1954), 273–286.

[30] J.-P. Eckmann, D. Ruelle: Ergodic theory of chaos and strange attractors, *Rev. Mod. Phys.* **57** (1985), 617–655.

[31] A. Speranza, V. Lucarini: Environmental Science: physical principles and applications, in *Encyclopedia of Condensed Matter Physics*, F. Bassani, J. Liedl, P. Wyder eds., Elsevier, Amsterdam, in press (2005).

[32] J.R. Holton: *An Introduction to Dynamic Meteorology*, Academic Press, San Diego, 1992.

[33] B.J. Hoskins, M.E. McIntyre, A.W. Robertson: On the use and significance of isentropic potential vorticity maps, *Quart. J. R. Met. Soc.* **111** (1985), 877–946.

[34] V. Lucarini, J.J. Saarinen, K.-E. Peiponen, E. Vartiainen: *Kramers-Kronig Relations in Optical Materials Research*, Springer, Heidelberg, 2005.

[35] I.M. Held, A.Y. Hou: Nonlinear Axially Symmetric Circulations in a Nearly Inviscid Atmo-

sphere, *J. Atmos. Sci.* **37** (1980), 515–533

[36] Yu. Kuznetsov: *Elements of Applied Bifurcation Theory* (2nd ed.), Springer–Verlag (1998).

[37] H.L. Kuo: Dynamics of quasigeostrophic flows and instability theory, *Adv. Appl. Mech.* **13** (1973), 247–330.

[38] A.J. Simmons, B.J. Hoskins: The life cycles of some nonlinear baroclinic waves, *J. Atmos. Sci.* **35** (1978), 414–432.

[39] W.J. Randel, J.L. Stanford: The observed life cycle of a baroclinic instability, *J. Atmos. Sci.* **42** (1985), 1364–1373

[40] I.N. James, L.J. Gray: Concerning the effect of surface drag on the circulation of a baroclinic planetary atmosphere, *Quart. J. Roy. Meteor. Soc.* **112** (1986), 1231–1250.

[41] P.G. Drazin, W.H. Reid: *Hydrodynamic stability*, Cambridge University Press, Cambridge, 1981.

[42] Y. Pomeau, P. Manneville: Intermittent transition to turbulence in dissipative dynamical systems, *Comm. Math. Phys.* **74** (1980), 189–197.

[43] A. Brandstater, H. L. Swinney: Strange attractors in weakly turbulent Couette-Taylor flow, *Phys. Rev. A* **35** (1987), 2207–2220.

[44] H.W. Broer, C. Simó, R. Vitolo: Bifurcations and strange attractors in the Lorenz-84 climate model with seasonal forcing, *Nonlinearity* **15** (2002), 1205–1267.

[45] J.D. Farmer, J. Hart, P. Weidman: A Phase Space Analysis of Baroclinic Flow, *Physics Letters A* **91** (1982), 22–24.

[46] A. Randriamampianina, W.-G. Früh, P. Maubert, P.L. Read: DNS of bifurcations to low-dimensional chaos in an air-filled rotating baroclinic annulus, *preprint at* `http://www-atm.physics.ox.ac.uk/user/read/` (2005).

[47] H.W. Broer, G.B. Huitema, M.B. Sevryuk: *Quasi-periodic Motions in Families of Dynamical Systems, Order amidst Chaos*, Springer LNM **1645** (1996).

[48] H.W. Broer, C. Simó, R. Vitolo: Chaos and quasi-periodicity in diffeomorphisms of the solid torus, *preprint* `mp_arc` #05-107 (2005).

[49] H.W. Broer, C. Simó, J.C. Tatjer: Towards global models near homoclinic tangencies of dissipative diffeomorphisms, *Nonlinearity* **11** (1998), 667–770.

[50] J. Guckenheimer, G. Buzyna: Dimension measurements for Geostrophic Turbulence, *Phys. Rev. Lett.* **51(16)** (1983), 1438–1441.

[51] M. Hénon, Y. Pomeau: Two strange attractors with a simple structure, in *Turbulence and Navier-Stokes equations* **565** (1976), Springer-Verlag, 29–68.

[52] C. Simó: On the Hénon–Pomeau attractor, *J. Stat. Phys.* **21** (1979), 465–494.

[53] Y. Cao: The transversal homoclinic points are dense in the codimension-1 Hénon-like strange attractors, *Proc. Amer. Math. Soc.* **127** (1999), 1877–1883.

[54] L. Mora, M. Viana: Abundance of strange attractors, *Acta Math.* **171** (1993), 1–71.

[55] M. Viana: What's new on Lorenz strange attractors?, *Math. Intelligencer* **22-3** (2000), 6–19.

[56] V.I. Oseledec: A multiplicative ergodic theorem. Lyapunov characteristic numbers for dynamical systems, *Trudy Mosk. Mat. Obsc. (Moscow Math. Soc.)* **19** (1968), 19.

[57] J. Kaplan, J. Yorke: Chaotic behaviour of multidimensional difference equations, in Functional Differential Equations and Approximations of Fixed Points, *Springer LNM* (1979), 204–227.

[58] J.D. Farmer, E. Ott, and J.A. Yorke: The dimension of chaotic attractors, *Physica D* **7** (1983), 153–180.

[59] D. Ruelle: Deterministic chaos: the science and the fiction, *Proc. R. Soc. London A* **427** (1990), 241–248.

[60] Q. Wang, L.-S. Young: Strange Attractors with One Direction of Instability, *Comm. Math. Phys.* **218** (2001), 1–97.

[61] S.V. Gonchenko, I.I. Ovsyannikov, C. Simó, D. Turaev: Three-dimensional Hénon-like maps and wild Lorenz-like attractors, *preprint at* `http://www.maia.ub.es/dsg/2005`.

[62] L.A. Smith: Disentangling Uncertainty and Error: On the Predictability of Nonlinear Systems, in *Nonlinear Dynamics and Statistics*, A. Mees ed., Birkhauser, Boston (2000) 31–64.

[63] L.A. Smith: What might we learn from climate forecasts?, *Proc. Natl. Acad. Sci.* **99** (2002), 2487–2492.

[64] J.P. Boyd: *Chebyshev & Fourier Spectral Methods*, Lecture Notes in Engineering **49**, Springer-Verlag, Berlin, 1989.

[65] N. Nakamura: Momentum flux, flow symmetry, and the nonlinear barotropic governor, *J. Atmos. Sci.* **50** (1993), 2159–2179.

[66] P. Stone: Baroclinic adjustment, *J. Atmos. Sci.* **35** (1978), 561–571.

[67] D. Gottlieb, S.A. Orszag: *Numerical Analysis of Spectral Methods: Theory and Applications*, CBMS-NSF Regional Conference Series in Applied Mathematics **26**, SIAM Publications, Philadelphia, 1977.

[68] M. Frigo, S.G. Johnson: The Design and Implementation of FFTW3, Proceedings of the IEEE **93(2)**, 216–231 (2005). Invited paper, Special Issue on Program Generation, Optimization, and Platform Adaptation.

[69] L.F. Shampine, H.A. Watts, S. Davenport: Solving Non-stiff Ordinary Differential Equations

- The State of the Art, *SIAM Review* **18** (1976), 376–411.

[70] G. Benettin, L. Galgani, A. Giorgilli, J.-M. Strelcyn: Lyapunov characteristic exponents for smooth dynamical systems and for Hamiltonian systems; a Method for computing all of them, Part 2: numerical applications, *Meccanica* **15** (1980), 21–30.

[71] C. Simó: On the Analytical and Numerical Approximation of Invariant Manifolds, *Les Méthodes Modernes de la Mecánique Céleste (Course given at Goutelas, France, 1989)*, D. Benest and C. Froeschlé eds., Editions Frontières, Paris (1990), 285–329. Available at `www.maia.ub.es/dsg/2004/index.html`.